AGU PUBLICATIONS

Paleoceanography

RESEARCH ARTICLE
10.1002/2016PA002940

Key Points:
- Biotic changes, eutrophy, and weakening of water thermal stratification were more marked for ETM2
- Terrigenous dilution is linked to strengthening of hydrological cycle and enhanced weathering
- Biotic changes and environmental perturbations persisted during carbon isotope excursion recovery

Supporting Information:
- Supporting Information S1
- Table S2
- Table S3
- Table S4
- Table S5
- Table S6

Correspondence to:
R. D'Onofrio,
dnfrrt@unife.it

Citation:
D'Onofrio, R., V. Luciani, E. Fornaciari, L. Giusberti, F. Boscolo Galazzo, E. Dallanave, T. Westerhold, M. Sprovieri, and S. Telch (2016), Environmental perturbations at the early Eocene ETM2, H2, and I1 events as inferred by Tethyan calcareous plankton (Terche section, northeastern Italy), *Paleoceanography*, *31*, doi:10.1002/2016PA002940.

Received 25 FEB 2016
Accepted 20 AUG 2016
Accepted article online 24 AUG 2016

Environmental perturbations at the early Eocene ETM2, H2, and I1 events as inferred by Tethyan calcareous plankton (Terche section, northeastern Italy)

Roberta D'Onofrio[1], Valeria Luciani[1], Eliana Fornaciari[2], Luca Giusberti[2], Flavia Boscolo Galazzo[2], Edoardo Dallanave[3], Thomas Westerhold[4], Mario Sprovieri[5], and Sonia Telch[2]

[1]Dipartimento di Fisica e Scienze della Terra, Università di Ferrara, Ferrara, Italy, [2]Dipartimento di Geoscienze, Università di Padova, Padua, Italy, [3]Department of Earth and Environmental Science, Ludwig Maximilians University of Munich, Munich, Germany, [4]MARUM - Center for Marine Environmental Sciences, University of Bremen, Bremen, Germany, [5]Istituto per l'Ambiente Marino Costiero del Consiglio Nazionale delle Ricerche, Campobello di Mazzara, Italy

Abstract Several early Eocene hyperthermals have been recently investigated and characterized in terms of temperature anomalies and oceanographic changes. The effects of these climatic perturbations on biotic communities are much less constrained. Here we present new records from the Terche section (northeastern Italy) that, for the first time, integrates data on planktic foraminifera and calcareous nannofossils across three post-Paleocene-Eocene Thermal Maximum negative carbon isotope excursions (CIEs). The biomagnetostratigraphic framework generated at Terche allows us to confidently relate such CIEs to the Eocene Thermal Maximum 2 (ETM2), H2, and I1 events. Each of these events coincides with lithological anomalies characterized by significantly lower calcium carbonate content (marly units, MUs). We interpret these MUs as mainly linked to an effect of increased terrigenous dilution, as dissolution proxies do not display significant variations. Calcareous plankton assemblages change significantly across these events and radiolarians increase. Observed changes suggest that transient warming and environmental perturbations, though more intense during ETM2, occurred during each of the three investigated perturbations. Variations among calcareous plankton suggest increase in surface-water eutrophication with respect to the pre-event conditions, coupled with a weakening of the upper water-column thermal stratification. Higher nutrient discharge was related to intensification of the hydrological cycle as a consequence of the warmer climate. These conditions persisted during the early CIE recovery, implying slower recovery rates for the environment and biota than for the carbon cycle.

1. Introduction

The early Paleogene climate was characterized by abrupt, short-term global warming events, known as hyperthermals. The term "hyperthermal" was introduced by *Thomas et al*. [2000] to describe "intervals—during the early Paleogene—of extremely high temperatures and very low latitudinal sea surface temperature gradients during which the deep-intermediate oceans were dominated by waters derived from subtropical latitudes." The most extreme hyperthermal was the extensively studied Paleocene/Eocene Thermal Maximum (PETM or ETM1) [e.g., *Kennett and Stott*, 1991; *Zachos et al*., 2010; *McInerney and Wing*, 2011] at ~56 Ma [e.g., *Westerhold et al*., 2008]. Hyperthermals share similar characteristics, though with different magnitudes, such as negative excursions in $\delta^{18}O$ and $\delta^{13}C$ records [e.g., *Cramer et al*., 2003; *Littler et al*., 2014, and references therein] and evidence for dissolution of deep-sea carbonates due to lysocline rise [e.g., *Zachos et al*., 2005; *Leon-Rodriguez and Dickens*, 2010; *Hönisch et al*., 2012]. Nonetheless, the magnitude (>−3‰ $\delta^{13}C$ excursion in marine carbonates; 5–8°C of global warming) [e.g., *McInerney and Wing*, 2011] and duration (~170–230 kyr) [e.g., *Giusberti et al*., 2007; *Röhl et al*., 2007] of the PETM were unmatched among the hyperthermals so that it is considered as an exceptional perturbation of the climate and carbon cycle. Orbitally tuned records suggest that most of the early Paleogene hyperthermals and short-lived carbon isotope excursions, with the exception of the PETM, were paced by variations in Earth's orbit, with particular control in the long (405 kyr) and short (100 kyr) eccentricity bands [e.g., *Cramer et al*., 2003; *Lourens et al*., 2005; *Westerhold et al*., 2007, 2008, 2015; *Galeotti et al*., 2010; *Zachos et al*., 2010; *Littler et al*., 2014; *Lauretano et al*., 2015]. Variations in Earth's orbital parameters are believed to have induced repeated emissions of isotopically depleted CO_2 into the ocean-atmosphere system [*Lourens et al*., 2005; *Sexton et al*., 2011;

Kirtland-Turner et al., 2014], but the ^{13}C-depleted carbon reservoir along with the carbon cycle dynamics allowing such emissions remains uncertain [e.g., *Pagani et al*., 2006; *Zeebe et al*., 2009; *Dickens*, 2011; *Lunt et al*., 2011; *Sexton et al*., 2011; *De Conto et al*., 2012; *Kirtland-Turner et al*., 2014].

Among extra-PETM carbon isotope excursions (CIEs) the Eocene Thermal Maximum 2 (also referred as ELMO in *Lourens et al*. [2005] and H1 in *Cramer et al*. [2003]) at 54.02 Ma was the most intense, with a ~1‰ negative CIE in marine carbonates [e.g., *Stap et al*., 2009; *Galeotti et al*., 2010; *Leon-Rodriguez and Dickens*, 2010; *Littler et al*., 2014]. During the ETM2 ocean sea surface temperature warmed of approximately 3.5°C [*Sluijs et al*., 2009; *Stap et al*., 2010b], and precipitations increased at midlatitudes and in the Arctic region [*Nicolo et al*., 2007; *D'Haenens et al*., 2012, 2014; *Slotnick et al*., 2012; *Krishnan et al*., 2014]. Smaller negative CIEs, close to ~0.5‰, and with an average duration of 40–60 kyr punctuated the long-term warming trend started in the latest Paleocene and culminated into the Early Eocene Climatic Optimum and continued to occur later in the middle Eocene [e.g., *Cramer et al*., 2003; *Sexton et al*., 2011; *Kirtland-Turner et al*., 2014; *Luciani et al*., 2016]. There is a general consensus to refer the PETM, the ETM2, and the Eocene Thermal Maximum 3 (ETM3 or X/K; at 52.83 Ma) [*Röhl et al*., 2005; *Thomas et al*., 2006; *Westerhold et al*., 2015] as proper hyperthermals [e.g., *Nicolo et al*., 2007; *Zachos et al*., 2010; *Slotnick et al*., 2012]. However, there is no total agreement whether to extend this designation to the numerous other early Paleogene minima in $\delta^{13}C$ [e.g., *Zachos et al*., 2010; *Kirtland-Turner et al*., 2014].

Extensive research is being focused on characterizing the early Paleogene succession of extra-PETM negative CIEs in terms of geochemical variations, timing, and magnitude. However, relatively little effort has been devoted to investigate their biotic repercussions, environmental impact, and potential influence on biotic long-term evolution. In particular, the response of marine calcareous plankton to the early Paleogene carbon cycle perturbations is so far largely unconstrained due to the widespread occurrence of carbonate dissolution at deep-sea sites [e.g., *Stap et al*., 2009; *Leon-Rodriguez and Dickens*, 2010; *Dedert et al*., 2012; *Gibbs et al*., 2012; *Jennions et al*., 2015]. Nonetheless, calcareous plankton plays a crucial role in both the carbon cycle and in reconstruction of paleoceanographic conditions, thanks to the recognized paleoecological affinities of most Eocene genera or species. Only a few scattered oceanic records are available to date (Figure 1). Most of the calcareous nannofossil assemblages from oceanic sites (Ocean Drilling Program, ODP) are affected by differential dissolution. They record both decrease (North Pacific Site 1209) and increase (South Atlantic, Site 1265) in primary productivity during the ETM2 [*Dedert et al*., 2012; *Gibbs et al*., 2012]. The sole ETM2 planktic foraminiferal record, published to date, is provided by *Stassen et al*. [2012] from the shelf setting of the Dababiya section (Egypt), and it shows an increase of acarininids across the event.

Here we add new integrated biomagnetostratigraphic and geochemical data for the ETM2, H2, and I1 events as recorded at the Terche section (northeastern Italy, central western Tethys). We investigate planktic foraminiferal and calcareous nannofossil assemblages across these three subsequent post-PETM events with the aim to increase our understanding of the behavior of marine biota communities during abrupt warming episodes and of their resilience to periodic climate disruptions. We may also achieve insight on correspondences and dissimilarities among the investigated events, considering that they are not unanimously regarded as hyperthermals. Our calcareous plankton records present only minor signs of dissolution across the $\delta^{13}C$ minima, possibly representing the most genuine record available to date as regards the assemblages integrity. This study represents the first attempt to integrate and directly compare the responses of the main calcareous plankton groups to multiple post-PETM events of carbon cycle perturbations.

2. Settings, Stratigraphy, and Lithology

The Terche section (46°2′43.61″N, 12°4′47.78″E) is located in the Venetian Southern Alps (northeastern Italy), approximately 2 km south of Mel village (Belluno), and outcrops in correspondence of a Terche Creek right tributary (Figure S1 in the supporting information). Sedimentary rocks exposed in the study area are part of the local Upper Cretaceous-lower Eocene pelagic-hemipelagic succession, deposited in the Belluno Basin, a Mesozoic-Cenozoic paleogeographic unit of the Southern Alps [e.g., *Bosellini*, 1989]. The entire Terche section consists of more than 85 m of pink-reddish to green scaly calcareous marls and marly limestones, locally rhythmically organized, referred to as the Scaglia Rossa Formation. The section splits into two segments, here labeled A and B (Figure 2), by a tectonized and covered interval occurring at approximately 61 m from the base. The segment A is 63 m thick and presents in the upper portion a scarcely outcropping package (>3 m) of dark

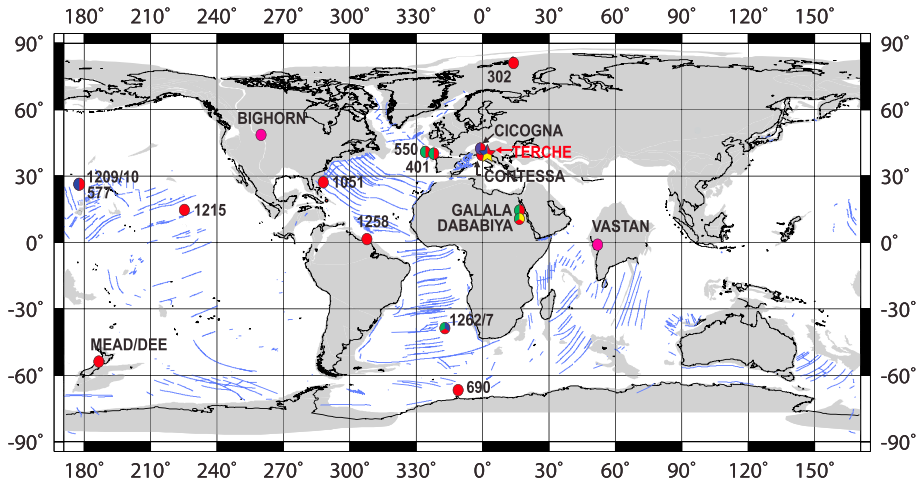

Figure 1. Earth at 54 Ma showing multiple locations where ETM2, H2, and I1 carbon isotope excursions have been documented in bulk carbonate or planktic and benthic foraminifera. These locations include the following: Ocean Drilling Program (ODP) Sites 1262 to 1267, 690, 1051 and Deep Sea Drilling Program (DSDP) sites 401 and 550 from the Atlantic Ocean [*Lourens et al.*, 2005; *Cramer et al.*, 2003; *Röhl et al.*, 2005; *Zachos et al.*, 2005, 2010; *Stap et al.*, 2009, 2010a, 2010b; *D'Haenens et al.*, 2012]; Integrated Ocean Drilling Program Site 302 from Artic Ocean [*Sluijs et al.*, 2009; *Schoon et al.*, 2011]; ODP sites 1209, 1210, 1215 and DSDP Site 577 from the Pacific Ocean [*Dedert et al.*, 2012; *Gibbs et al.*, 2012; *Leon-Rodriguez and Dickens*, 2010; *Cramer et al.*, 2003]; land sections from Mead and Dee Stream, New Zealand [*Hollis et al.*, 2005; *Nicolo et al.*, 2007; *Slotnick et al.*, 2012]; Bighorn Basin, North America [*Abels et al.*, 2012; *Chew*, 2015]; Vastan, India [*Clementz et al.*, 2011]; Italy (Contessa section, central Italy [*Galeotti et al.*, 2010; *Coccioni et al.*, 2012] and Cicogna sections, northeastern Italy [*Agnini et al.*, 2016]); Galala and Dababiya sections from Egypt [*Höntzsch et al.*, 2011; *Stassen et al.*, 2012]. Red color: locations where geochemical data are not coupled with biotic data from marine record; blue color: sites with data on calcareous nannofossils; green color: successions showing variations on benthic foraminifera; yellow color: data on planktic foraminifera; and pink color: terrestrial record. Note that the Terche section (star) is the only deep-sea record where the combined response from calcareous nannofossil and planktic foraminifera is given for the three post-PETM hyperthermals. Base map is from http://www.odsn/de/services/paleomap.html, paleolatitudes are modified according to www.paleolatitude.org model version 1.2 [*Van Hinsbergen et al.*, 2015].

red clayey marls corresponding to the clay marl unit (CMU), the regional lithological expression of the PETM main CIE [*Giusberti et al.*, 2007]. The segment B (~ 27 m thick) is the main focus of this paper and crops out with continuity. It is characterized by the presence of three reddish marly and clayey intervals (marly units, MUs) which thickness varies from 1.1 to 1.5 m. Such lithological anomalies, here labeled as MU1, MU2, and MU3 (from the base to the top), interrupt the predominantly calcareous marl lithology.

3. Methods

3.1. Planktic, Benthic Foraminifera, and Radiolarians

Planktic foraminifera and radiolarians were analyzed on 78 samples spanning the lower Eocene portion of the Terche section containing the three post-PETM MUs (segment B; Figure 2). The sample spacing was 2–10 cm across the MUs and 40–60 cm below and above. Foraminifera were extracted using different techniques depending on the different lithologies. Specifically, soft marly samples were processed with the hydrogen peroxide method, whereas limestone and indurate marl were treated with the "cold acetolyse" technique of *Lirer* [2000]. For both these methods, 50–100 g of dry sediment was crushed into small fragments of about 5 mm in diameter. The disintegration is carried out by immersion of the obtained fragments in a solution of hydrogen peroxide (H_2O_2) diluted from 10% to 35% or a solution of acetic acid (CH_3COOH) diluted to 80%. In most cases, additional treatment with pure surface-tension-active chemical products (e.g., neo-Desogen) was required in order to eliminate or reduce clumps of residues or incrustations on the test surface. In some cases a gentle ultrasonic bath (e.g., low frequency at 40 kHz for less than 15 s) further improved the cleaning of the tests. All the samples were washed and sieved using a 63 μm mesh size.

Planktic foraminifera have been analyzed by counting the relative abundance of genera and groups of genera on a population of about 300 specimens in the greater than or equal to 63 μm size fraction on representative splits of washed residues. Counts are expressed in percentage. Groups of genera were combined

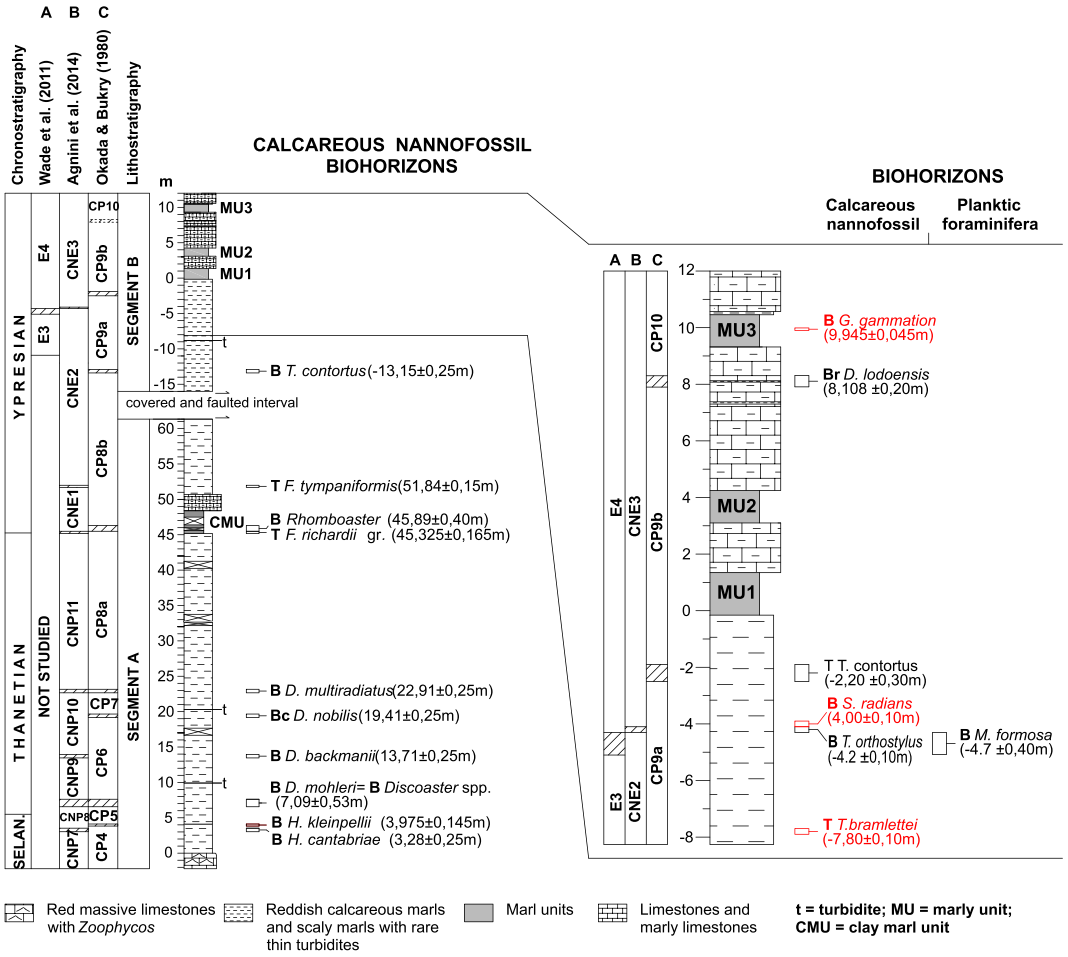

Figure 2. Stratigraphic log of the entire Terche section with the close-up of the segment B focus of this study. Level 0 m corresponds to the level with the lowest $CaCO_3$ value within MU1 (see Figure 4). Planktic foraminiferal and calcareous nannofossil main (in black) and secondary (in red) biohorizons are shown and discussed in the text, together with the zonal attribution according to *Wade et al*. [2011], for the former, and *Agnini et al*. [2014] and *Okada and Bukry* [1980] for the latter. The unfilled rectangle near the biohorizons indicates the uncertainty derived from the sample spacing. The same uncertainty is represented in the zonal scheme columns by the striped bands. In the next figures representing the studied segment, the zonal boundaries are placed at the middle level between two successive samples. The abundances of calcareous nannofossil zonal markers are given in Figure S2.

according to the ecological affinities of the different taxa [*Pearson et al*., 2006, and references therein]. In the *Subbotina* group were included the genera *Subbotina*, *Parasubbotina*, *Paragloborotalia*, and *Globorotaloides*, while the chiloguembelinids comprise *Chiloguembelina* and *Zeauvigerina*. Foraminiferal taxonomic criteria adopted in this study are from *Olsson et al*. [1999] and *Pearson et al*. [2006]. Planktic foraminiferal biostratigraphy is according to *Wade et al*. [2011].

Benthic foraminiferal assemblage was analyzed for paleobathymetric indications between –8 and +11 m (Figure 2). Analyses were performed on the ≥63 μm size fraction on representative splits of washed residues (obtained using a precision microsplitter) containing a number of benthic foraminifera greater than or equal to 400 specimens.

Radiolarian abundance was estimated as relative percentage with respect to planktic foraminifera on a population of at least 300 specimens.

3.2. Calcareous Nannofossils

Ninety-one samples were prepared from unprocessed material as smear slides and examined using a light microscope at ~1250X magnification. Samples for calcareous nannofossil analysis have been collected both

from segment A (at spacing variable from 2.0 m to 0.5 m) and B (at spacing variable from 0.5 m to 0.05 m) (Table S2) to preliminarily characterize biostratigraphically the entire section and to evaluating the abundance and the state of preservation of the calcareous nannofossil assemblages. The presence or absence of index species was assessed by mean of quantitative and semiquantitive countings following the methods developed by *Thierstein et al*. [1977], *Backman and Shackleton* [1983], *Rio et al*. [1990a], and *Gardin and Monechi* [1998]. Specifically, (1) the abundance of selected species was calculated taking into account at least 300 specimens; (2) a prefixed number of taxonomically related forms was counted, e.g., 100 sphenoliths; (3) index species were counted in a prefixed area (1 mm^2); and (4) specimens of rare but biostratigraphically useful species (i.e., discoasterids and *Tribrachiatus*) were counted in an area of about 6–7 mm^2, which is roughly equivalent to three vertical traverses.

Calcareous nannofossil zonations are according to *Okada and Bukry* [1980] and *Agnini et al*. [2014].

3.3. Magnetostratigraphy

The magnetic mineralogy and rock-magnetic properties of the Paleogene sediments of the Belluno Basin have been extensively investigated by *Dallanave et al*. [2009, 2010, 2012a, 2012]. In particular, detailed paleomagnetic and rock-magnetic study of the lower Eocene sediments of the Cicogna section [*Dallanave et al*., 2009, 2010] revealed that the dominant magnetic mineral is detrital hematite, which coexist with minor maghemite. The occurrence of magnetite is limited to gray-greenish levels and spots of early diagenetic origin, commonly associated with bioturbation.

We collected a total of 46 paleomagnetic core samples across 13 stratigraphic meters of the Terche section (Figure 2, segment B). Samples were drilled with a gasoline-powered drill and oriented with a magnetic compass. From each core we obtained a standard ~11 cm^3 specimen for paleomagnetic directional analyses. All the oriented specimens were thermally demagnetized up to 675°C with steps of 50°C, reduced to 25°C from 500°C onward. The natural remanent magnetization (NRM) was measured after each demagnetization step using a 2-G Enterprises superconducting magnetometer placed in a shielded room at the Paleomagnetic laboratory of the Ludwig-Maximilians University (Munich, Germany). The component structure of the NRM was examined by means of vector endpoint demagnetization diagrams [*Zijderveld*, 1967], and the principal component analyses of *Kirschvink* [1980] have been applied on linear segments of the demagnetization paths to isolate the NRM components. Mean directions and associated confidence limits were calculated using the spherical statistics of *Fisher* [1953]. Directional analyses have been performed with the PaleoMag software compiled by *Jones* [2002]. Scattered magnetic component directions have been generally isolated from room temperature up to ~200°C. After the removal of this spurious component, a characteristic remanent magnetization (ChRM) component of the NRM linearly trending to the origin of the demagnetization axes has been isolated up to 600–675°C in 70% ($^{32}/_{46}$) of the specimen.

3.4. Stable Isotope and $CaCO_3$ Analyses

Bulk carbon and oxygen stable isotopes and $CaCO_3$ analyses were performed on 150 samples collected from −10.90 m to +11.37 m (segment B; Figure 2) with a mean spacing of 20 cm. The sample spacing was increased (2–10 cm) across the MUs. Stable isotope analyses were carried out with an automated continuous flow carbonate preparation GasBench II device [*Spötl and Vennemann*, 2003] and a Thermo Electron Delta Plus XP mass spectrometer at the IAMC-CNR isotope geochemistry laboratory of Naples. The acidification of the samples was performed at 50°C. An internal standard (Carrara Marble with $\delta^{18}O = -2.43‰$ versus Vienna Pee Dee Belemnite and $\delta^{13}C = 2.43‰$ versus VPDB) was run every six samples, and the NBS19 international standard was measured every 30 samples. Standard deviations of carbon and oxygen isotope measures were estimated to be 0.1 and 0.08‰, respectively, on the basis of ~200 samples that were measured three times. All of the isotope data are reported in δ‰ versus VPDB.

$CaCO_3$ content was measured with the electronic gas volumetric GEO-RS Calcimeter (analytical precision of ± 0.2%) at the University of Ferrara. All the samples were dried, crushed, and then pulverized. Calcimetric analyses were performed on 0.50 g (±0.001 g) of pulverized samples through the reaction deriving from the treatment with 5 ml hydrochloric acid solution (HCl) diluted to 10%. Carbonate weight percentage was obtained as a function of the increase in pressure due to the release of carbon dioxide (CO_2), according to the following relation: $CaCO_3 + 2HCl \rightarrow Ca + 2Cl + H_2O + CO_2$. Every 10 determinations the instrument was calibrated using 0.500 g of pure Carlo Erba RPE calcium carbonate powder as standard.

3.5. Dissolution and Calcareous Plankton Preservation Proxies

Hyperthermals are frequently associated with dissolution of deep-sea carbonates due to the rise of the CCD/lysocline [e.g., *Zachos et al*., 2005; *Stap et al*., 2009]. Planktic foraminiferal tests tend to break into fragments as they dissolve whereas benthic foraminifera are less prone to dissolution [e.g., *Berger*, 1970, 1973; *Bé et al*., 1975; *Hancock and Dickens*, 2005; *Leon-Rodriguez and Dickens*, 2010; *Nguyen and Speijer*, 2014]. Dissolution can therefore modify the composition of the planktic foraminiferal assemblages [e.g., *Berger*, 1970; *Bé et al*., 1975; *Thunell and Honjo*, 1981; *Petrizzo et al*., 2008; *Nguyen et al*., 2009, 2011].

In order to assess possible carbonate dissolution effects we adopted here three different proxies based on foraminifera:

1. *The fragmentation index (F index)*. The *F* index was calculated following *Berger* [1970] and *Petrizzo et al*. [2008] as the ratio between fragments or partially dissolved planktic foraminiferal tests versus entire tests on ~300 individuals. Fragmented foraminifera include specimens showing notable deterioration, missing chambers, and substantial breakage.
2. *The planktic over benthic ratio (P/B)*. The *P/B*, usually adopted with some cautions for paleobathymetric estimations [e.g., *Murray*, 1976; *Van der Zwaan et al*., 1990], can be also applied as a dissolution index in absence of significant bathymetric variations. The *P/B* index was calculated on ~300 specimens and is here expressed as $100 * P/(P + B)$.
3. *The weight percent coarse fraction (WPCF)*. The WPCF was obtained from the ratio of the dry washed residue (≥38 μm size fraction) to the bulk dry sediment [*Hancock and Dickens*, 2005]. In pelagic sediments not affected by dissolution, the WPCF can give indication about planktic foraminiferal productivity [*Hancock and Dickens*, 2005]. However, the WPCF can be largely controled by dissolution of planktic foraminifera as well, which is strongly coupled to the depth of the regional lysocline [e.g., *Berger et al*., 1982].

Calcareous nannofossil assemblages can be altered as well by dissolution that can selectively affect the different genera and species [e.g., *Adelseck et al*., 1973; *Bornemann and Mutterlose*, 2008; *Dedert et al*., 2012, 2014]. The calcareous nannofossil assemblages influenced by dissolution show low number of species accompanied by high abundances of dissolution-resistant taxa [*Bornemann and Mutterlose*, 2008]. The genus *Toweius* is one of the most fragile forms among the early Paleogene taxa [e.g., *Dedert et al*., 2012]. In particular, dissolution first affects the delicate structure of the central area of *Toweius*, thus preventing the identification of the different species. On the contrary, *Discoaster* has been considered as a dissolution-resistant taxon [e.g., *Adelseck et al*., 1973; *Rio et al*., 1990b; *Agnini et al*., 2007a]. A further aspect influencing the calcareous nannofossil preservation is related to the diagenesis that can induce overgrowth [e.g., *MacKenzie and Wise*, 1983; *Dedert et al*., 2014].

In order to evaluate the effects of carbonate dissolution and overgrowth on the calcareous nannofossil assemblages at Terche we have applied the following proxies:

1. *The species richness (diversity)*. Species richness is influenced, besides evolution, by both dissolution and overgrowth. Considering that no major turnovers in calcareous nannofossils are documented across the stratigraphic interval here investigated, low number of species can indicate strong dissolution/overgrowth and vice versa.
2. *Qualitative estimate of etching (Q_E) based on the modified scales from Roth and Thierstein* [1972] *and Roth* [1983]. Here we assess five degrees of etching on the basis of the coccolith outline preservation, the state of delicate structures, and the abundance of small placoliths that are considered as highly dissolution prone [*Adelseck et al*., 1973] (Table S1.1).
3. *Qualitative estimate of five degrees in overgrowth (Q_O) according to a modified scale from Dedert et al*. [2014] (Table S1.2). These degrees refer to the specimen thickness and to the differences of the coccolith surfaces from those biogenically sculpted.
4. *The relative percentage of the Toweius species with central area well preserved versus the total Toweius, included the unrecognizable specimens of this genus, i.e., the forms where the central area preservation does not allow the species identification ($T_{species}$)*. High values of the proxy indicate absence of dissolution or slight dissolution. On the contrary, low values suggest strong dissolution.
5. *The relative percentage of Toweius over that of Discoaster (T/D)*. This ratio is introduced here as proxy of dissolution. High values of T/D suggest low degree of dissolution and vice versa.

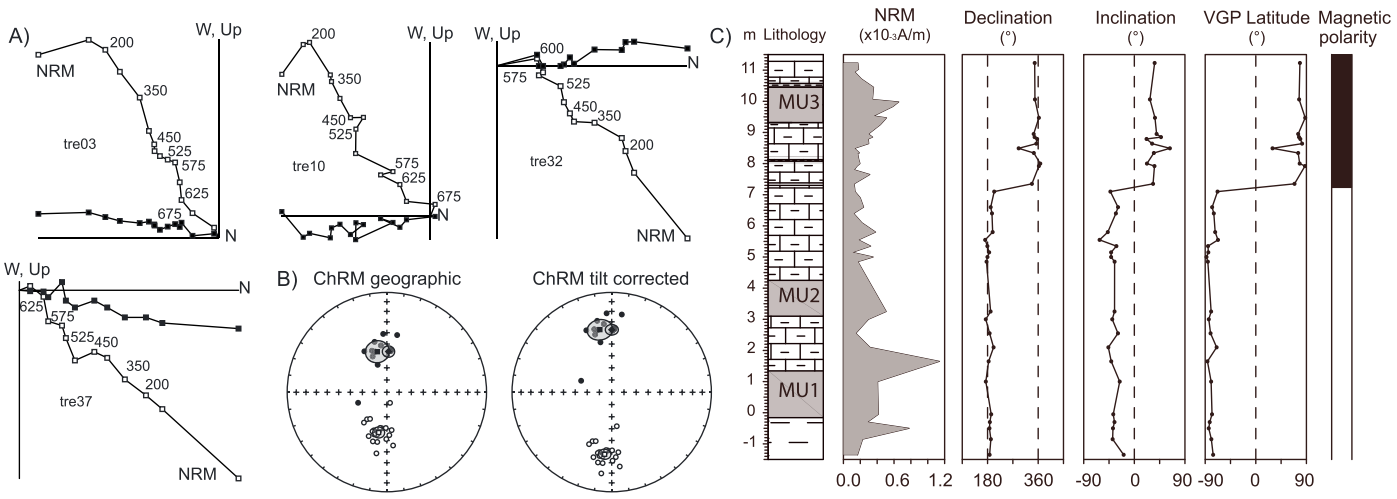

Figure 3. Paleomagnetic results from the Terche section. (a) Representative vector end-point demagnetization diagrams for the Terche specimens, plotted in geographic coordinates. Open (closed) squares represent vector end-point projections onto the vertical (horizontal) plane. Demagnetization steps are in °C. (b) Equal area projection of the characteristic remanent magnetization (ChRM) directions in geographic (left) and tilt-corrected (right) coordinates; black (white) data represent down (up) pointing directions. Black and white squares are average directions plotted with the associated $\alpha 95$ cone of confidence. Black diamonds are the average directions, with associated $\alpha 95$ cone of confidence, obtained inverting all ChRM directions on a common north pointing polarity. (c) Magnetic polarity stratigraphy of the Terche section. From left to right, lithostratigraphy and thickness, intensity of the natural remanent magnetization (NRM), declination and inclination of the characteristic remanent magnetization (ChRM) directions in tilt-corrected coordinates, virtual geomagnetic poles (VGP) latitude, and derived magnetic polarity stratigraphy; black and white bands represent, respectively, normal and reverse magnetic polarity zones. For lithological symbols see Figure 2.

4. Results

4.1. Calcareous Plankton Biostratigraphy

Calcareous plankton is abundant and well diversified in all the samples investigated. Planktic foraminifera at the segment B of Terche are relatively well preserved, though recrystallized and partially filled by calcite, thus allowing the identification at the species level. The main planktic foraminiferal event recorded is the base (B) of *Morozovella formosa* that identifies the boundary between the Zones E3/E4 [*Wade et al*., 2011] at −4.70 ± 0.40 m (Figure 2). The zonal marker is quite rare at the level of its appearance. The B of *Morozovella aragonensis* that marks the E4/E5 zonal boundary was not recorded in the studied interval.

All the calcareous nannofossil marker species used to define the zonal boundaries of *Okada and Bukry* [1980] and *Agnini et al*. [2014] are present. The entire Terche section encompasses the Zones CNP7 to CNE3 of *Agnini et al*. [2014] and CP4 to CP10 of *Okada and Bukry* [1980] (Figure 2). Nannofossils are generally well diversified, and their preservation ranges from poor to moderate, with variable degrees of overgrowth and recrystallization. Reworked forms are rare, except for the CMU at the Thanetian-Ypresian boundary and for the Ypresian MUs belonging to the segment B where reworked Cretaceous specimens become common to abundant. The segment B of Terche section spans Zones CP8 to CP10 of *Okada and Bukry* [1980] and Zones CN2 to CN3 pars of *Agnini et al*. [2014]. The main calcareous nannofossil biohorizons are described below in stratigraphic order, from the oldest to the youngest (Figure 2); their relative abundances are shown in Figure S2 and Table S2. The relative abundances of species markers of segment A are shown in Figure S3 and Table S2.

1. *Base of Tribrachiatus contortus*. The B of *T. contortus*, at −13.15 ± 0.25 m, defines the lower boundary of Zone CP9a [*Okada and Bukry*, 1980]. *T. contortus* shows a discontinuous distribution, and it is very rare in its initial range. A marked increase in abundance of the species occurs at −10.10 ± 0.10 m.
2. *Base of Tribrachiatus orthostylus and top (T) of T. contortus*. The B of *T. orthostylus* marks the lower boundary of Zone CNE3 at −4.2 ± 0.10 m. The increase of this species occurs concomitantly with the decrease of *T. contortus*, the disappearance of which, at −2.2 ± 0.30 m, identifies the CB9a-CP9b boundary (or base of NP11), consistently with previous data [*Agnini et al*., 2007, and references therein; *Dallanave et al*., 2009; *Agnini et al*., 2014].
3. *Base rare (Br) of Discoaster lodoensis*. The appearance of *D. lodoensis* is used to mark the base of Zones NP12 and CP10 [*Martini*, 1971; *Okada and Bukry*, 1980]. In the studied material, *D. lodoensis* appears with rare teratological morphotypes (seven and eight-rayed specimens) within Zone CNE3 in agreement with

Table 1. ChRM Directions from the Terche Section[a]

		Geographic Coordinates				Tilt-Corrected Coordinates			
N	MAD	*k*	α_{95}	DEC	INC	*k*	α_{95}	DEC	INC
				Normal Polarity Directions					
12	14.1 ± 5.4	20.5	9.4	346.8	55.5	20.7	9.3	349.3	36.2
				Reverse Polarity Directions					
20	7.3 ± 6.7	49.8	4.7	191.4	−56.0	51.8	4.6	186.5	−37.4
				Reverse and Normal Polarity Directions					
32	9.9 ± 7.0	28.6	4.8	2.3	56.4	29.2	4.8	0.1	37.3

[a]Characteristic remanent magnetization (ChRM) directions from the Terche section. *N* = number of specimens; MAD = maximum angular deviation (deg); *k* = *Fisher* [1953] precision parameter of the mean ChRM direction; α_{95} = *Fisher* [1953] confidence angle (deg) of the mean ChRM direction; and DEC and INC = declination and inclination of the mean ChRM directions.

Agnini et al. [2014]. This rare presence allows us to determine the Br of *D. lodoensis* that probably corresponds to the B of *D. lodoensis* according to *Martini* [1971] and *Okada and Bukry* [1980].

We highlight in Figure 2 the following supplementary events: T of *Tribrachiatus bramlettei*, B of *Sphenolithus radians*, and B of *Girgisia gammation*. The position of the two first events is in good agreement with previous studies [e.g., *Agnini et al*., 2006, 2007; *Dallanave et al*., 2009]. In particular, the B of *S. radians* virtually coincides at Terche with the B of *T. orthostylus* at CNE2-CN3 boundary. Our data substantiate that the B of *G. gammation* is a useful event to subdivide Zone CP9b [*Agnini et al*., 2006, 2007, 2014; *Dallanave et al*., 2009].

4.2. Magnetostratigraphy

At Terche, the intensity of the NRM ranges from 1.08×10^{-4} to 1.14×10^{-3} Am^{-1}, with an average value of 3.03×10^{-4} Am^{-1} (Figure 3), in agreement with the data from the coeval part of the Cicogna section [*Dallanave et al*., 2009, 2010, 2012]. The unblocking temperature indicates a magnetization carried by hematite, in agreement with the results obtained from the Cicogna section sediments. The ChRM directions are organized in two modes oriented north down and south up (Figure 3 and Table 1), which shallow of 19° after correction of a homoclinal 19° bedding tilt dipping 356°E. In tilt corrected coordinates the two modes depart from antipodality of 13.8°, failing the reversal test performed using the procedure of *Watson* [1983] (V_w = 12.0, $V_{critical}$ = 6.4). Inverting all ChRM directions to a common north down pointing polarity, we obtained the tilt-corrected mean direction indicated in Table 1.

We determined the virtual geomagnetic pole (VGP) position associated to each ChRM direction. The latitude of the VGPs, relative to the mean paleomagnetic north pole has been used to interpret the magnetic polarity stratigraphy [*Lowrie and Alvarez*, 1977; *Kent et al*., 1995]. Positive and negative relative VGP latitudes have been interpreted as reflecting, respectively, normal and reverse magnetic polarity. These data, together with the declination and the inclination of the ChRM directions, are shown in Figure 3. The Terche section is characterized by reverse magnetic polarity up to 7.23 m and by normal magnetic polarity stratigraphically upward. Integration with biostratigraphic data allows us to correlate this level with the C24r-C24n.3n Chron boundary (Figure 3).

4.3. $CaCO_3$ and Stable Isotope Record

The $CaCO_3$ Terche record is characterized by a slight increasing trend upward (from mean values of 55% to 64%) interrupted by three major drops corresponding to MUs (Figure 4 and Table S3). The minimum contents of 21%, 40%, and 37% are reached at +0.08 m, +3.5 m, and +9.43 m, respectively. In parallel with the carbonate drops three negative CIEs are recorded. The stratigraphically lower two shifts (~0.5‰) occur at +0.2 m and +3.8 m in the uppermost part of Chron C24r. The third ~0.5‰ CIE is recorded at +9.3 m within the base of sub-Chron C24n.3n (Figure 4 and Table S3). The $\delta^{13}C$ of the studied section records a number of wiggles that are not associated with lithological changes (Figure 4 and Table S3). By providing a three-point running average of the carbon isotope data, single-overprint outliers are dampened. A rather pronounced negative change of ~0.5‰ in the $\delta^{13}C$ profile is located at ~ −2.10 m. This shift has been observed at the same stratigraphic position at the nearby Cicogna section [*Agnini et al*., 2016] and at the ODP Sites 1262 and 1265 [*Stap et al*., 2010b].

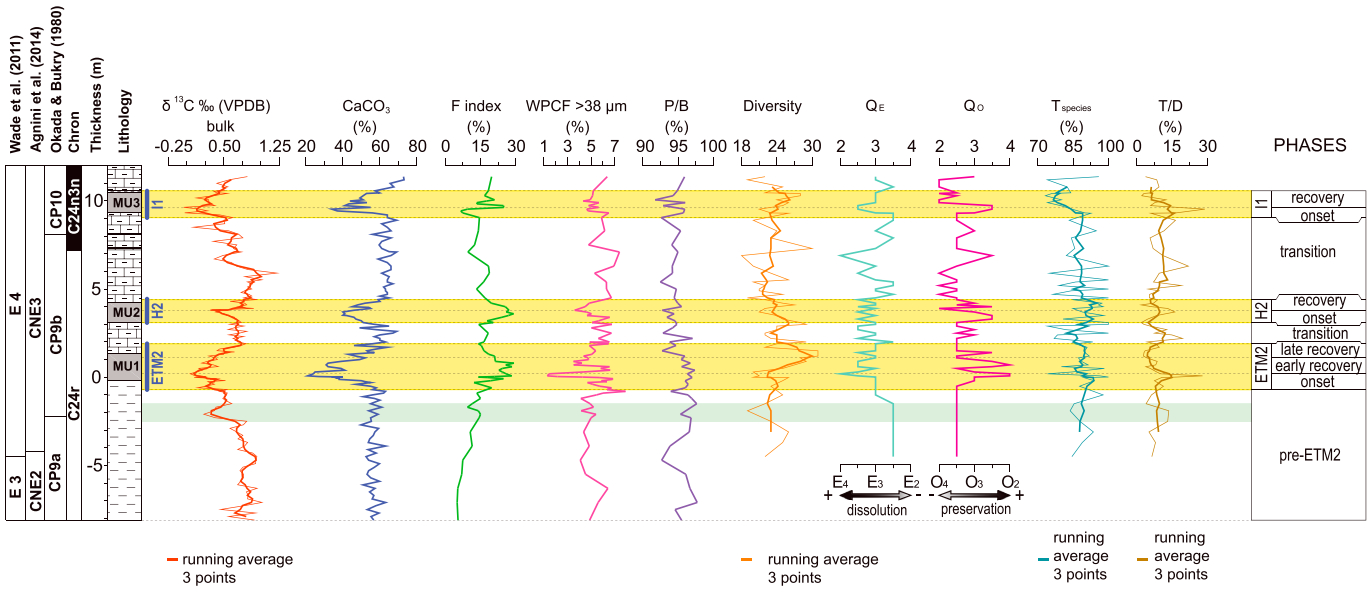

Figure 4. Curves showing the foraminiferal dissolution proxies and the calcareous nannofossil indices for dissolution and preservation (see text for adopted methods and discussion) plotted against the carbon stable-isotope record and the percentage of $CaCO_3$ at the Terche section. The foraminiferal dissolution proxies are the following: fragmentation index (*F* index), weight percent coarse fraction (WPCF), and plankton benthos ratio (*P*/*B*). The calcareous nannofossil dissolution indices are the following: species richness (diversity), qualitative estimation of etching (Q_E), relative percentage of the *Toweius* species with central area well preserved ($T_{species}$) versus all the species of *Toweius* (included the forms unrecognizable at species level), and *Toweius* (dissolution prone) *Discoaster* (dissolution resistant) ratio (T/D). The qualitative estimation of overgrowth (Q_O) is considered as a preservation proxy (see text). The yellow bands highlight the ETM2, H2, and I1 intervals as defined by the carbon cycle perturbations and expressed through the $\delta^{13}C$ shifts. We distinguish here 10 phases on the basis of the $\delta^{13}C$ curve variations. Pre-ETM2: interval below the negative CIE onset (from −8.1 m to −0.7 m). ETM2 onset: interval between the ETM2 CIE base and the level of the most negative $\delta^{13}C$ peak (from −0.7 m to +0.2 m). ETM2 early recovery: interval comprised between the ETM2 CIE peak to +1.1 m level. ETM2 late recovery: interval between + 1.1 m level and ETM2 CIE top, i.e., the level where the $\delta^{13}C$ curve returns to the pre-excursion values (+1.9 m). Similarly, we identify the onset of the H2 and I1 as corresponding to the interval between the base of the H2 and I1 CIEs and the levels of the most negative peaks (respectively, from +3.1 m to +3.8 m and from +9.0 m to +9.6 m). Due to the lower thickness of the interval corresponding to the H2 and I1 CIEs, we distinguish a unique recovery phase for each event (from + 3.8 m to +4.4 m and from +9.6 m to +10.6 m, respectively). Transitions between the ETM2-H2 and H2-I1: intervals of the $\delta^{13}C$ curve comprised between the negative shifts linked to the events (from +1.9 m to + 3.1 m and +4.4 m to +9.0 m). The light green band underlines a pre-ETM2 minimum in carbon stable isotopes (see text). For lithological symbols see Figure 2.

The $\delta^{18}O$ values widely fluctuate in the intervals comprised from –8.10 m to –2.50 m (–6.97‰ to –2.05‰) and from +6.5 m to +11.4 m (–6.16‰ to –1.03‰). Less pronounced variations are recorded from –2.30 m to +6.30 m where the $\delta^{18}O$ show a mean increase since values oscillate between –3.08‰ and –0.79‰.

4.4. Variation in Dissolution Proxies

The *F* index displays generally low background values close to 10%. A moderate increase in fragmented foraminiferal tests occurs within the MUs, up to ~29% (MU1 and MU2) and 25% (MU3), close to the negative peaks in $\delta^{13}C$ and the CaCO3% drops (Figure 4 and Table S4). According to our qualitative evaluation, partly dissolved and fragmented planktic foraminiferal tests appear proportional to the genera percentages with no dominance of a particular genus. The WPCF at Terche varies between 1% to 8%. The most evident fluctuations are recorded within the MU1 where the WPCF shows the minimum value. The *P*/*B* records minor fluctuations around the value of 95% ranging between 91% and 98.5% (Figure 4 and Table S4). The calcareous nannofossil diversity index (Figure 4 and Table S4) varies from 31 to 18 with a median of 24. Changes in the diversity curve are not directly correlated with the carbonate content and $\delta^{13}C$ curves. The lowest values (18–19 taxa) are indeed not associated with $CaCO_3$ and/or $\delta^{13}C$ minima (Figure 4 and Table S4). The Q_E curve (Figure 4) shows throughout values that generally correspond to moderately dissolved coccoliths ($Q_E \sim 3$). A heavily etched assemblage (Q_E 2, Plate S1) has been observed at the MU1 in coincidence of *F* index and WPCF variations at the $\delta^{13}C$ negative peak. Overgrowth did not severely affect the Terche calcareous nannofossil assemblages that appear even best preserved within the MUs (Q_O; Figure 4, Table 4, and Plate S1). A slight deterioration, though not steady, occurs in two segments of the upper part of the section (from +3.9 m to +5.9 m and from +9.9 m to +11.2 m). The $T_{species}$ curve shows high values fluctuating from 100% to ~ 75% with a mean of ~ 90%. In order to better highlight the general pattern a three-point running average of the $T_{species}$ has been performed (Figure 4 and Table S4).

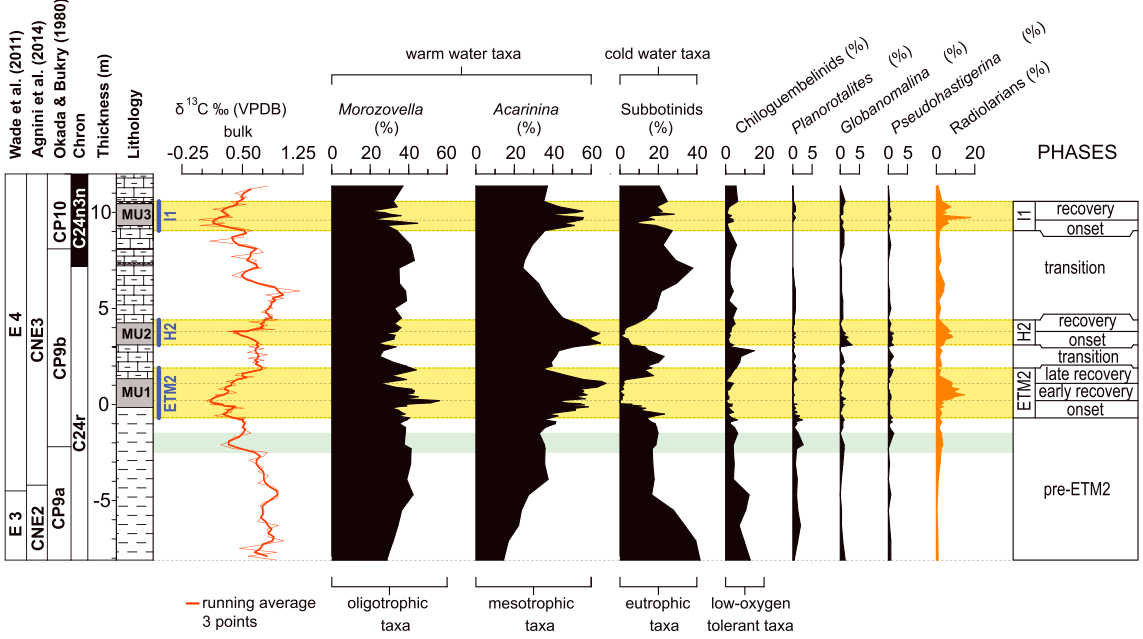

Figure 5. Changes in relative abundance of planktic foraminiferal genera (≥63 μm fraction) across the analyzed segment of the Terche section, plotted against carbon stable isotopes, biomagnetostratigraphy and radiolarian abundance. The *Subbotina* group includes, beside *Subbotina*, the ecologically similar genera *Parasubbotina*, *Paragloborotalia* and *Globorotaloides* [e.g., *Pearson et al.*, 2006]. Chiloguembelinids include the genera *Chiloguembelina* and *Zeauvigerina*. The yellow bands highlight the ETM2, H2, and I1 intervals expressed by the $\delta^{13}C$ negative shifts. We identify 10 phases on the basis of the $\delta^{13}C$ curve variations (see Figure 4 and discussion in the text). The light green band underlines a minimum in carbon stable isotopes (see discussion in the text). For lithological symbols see Figure 2.

Decreases of $T_{species}$ values are recorded within the MU1 and MU3 whereas across the MU2 the running average profile highlights a slight increase. The *T/D* curve displays mean values of 9% with peaks of ~30% at the MU1 and MU3.

4.5. Changes in Foraminiferal Assemblages and Radiolarian Abundance

The early Eocene genera typical of subtropical-temperate latitudes are represented at the Terche section (Figure 5 and Table S5). The mixed-layer dwelling warm-index acarininids and morozovellids and the thermocline-dwelling cold-index subbotinids [e.g., *Boersma et al.*, 1987; *Pearson et al.*, 1993, 2006] are the most abundant forms with a mean respective abundance of 45%, 35%, and 20% (Figure 5). The mean relative abundance of acarininids shows a long-term increase from the base to the top of the section. This is superimposed to the major fluctuations recorded within the MUs (Figure 5). The acarininid highest abundance (68%) is recorded close to the top of the MU1 at +1.2 m. Prominent peaks are recorded also within the MU2 and MU3 (~56%). These marked increases are associated with a slight reduction in acarininid test size, with specimens becoming very rare to absent in the >300 μm size fraction. Subbotinid abundance fluctuates in antiphase with acarininids. Within this group, the genus *Subbotina* is dominant whereas *Parasubbotina*, *Paragloborotalia*, and *Globorotaloides* constitute all together minor components throughout. Subbotinid strong reductions in relative abundance or even virtual absence are recorded within the MUs (Figure 5). Specifically, within the MU1 subbotinids record the lowest mean value of the entire section (~1.6%), and they temporarily disappear in coincidence of the maximum negative $\delta^{13}C$ peak recorded at +0.2 m. A marked drop in subbotinids is documented within the MU2 as well, where their abundance is reduced to ~1%. The MU3 records a less pronounced decrease in subbotinids (8%), but their lowest percentages again coincide with the lowest $\delta^{13}C$ values. Morozovellid abundance records less marked changes. Within the MUs, this group displays brief positive peaks that are particularly evident at the base of MU1 and MU3 (56% and 45%, respectively), followed by moderate decreases in abundance. Their rapid increase at the base of MU1 coincides with a significant decrease in test size, with specimens becoming virtually absent in the >250 μm size fraction, while dominating the fraction comprised between 150 μm and 250 μm. Chiloguembelinids at Terche present generally low abundances, having mean values of ~4% throughout the section (Figure 5 and Table S5) and are mostly represented by *Chiloguembelina* with respect to

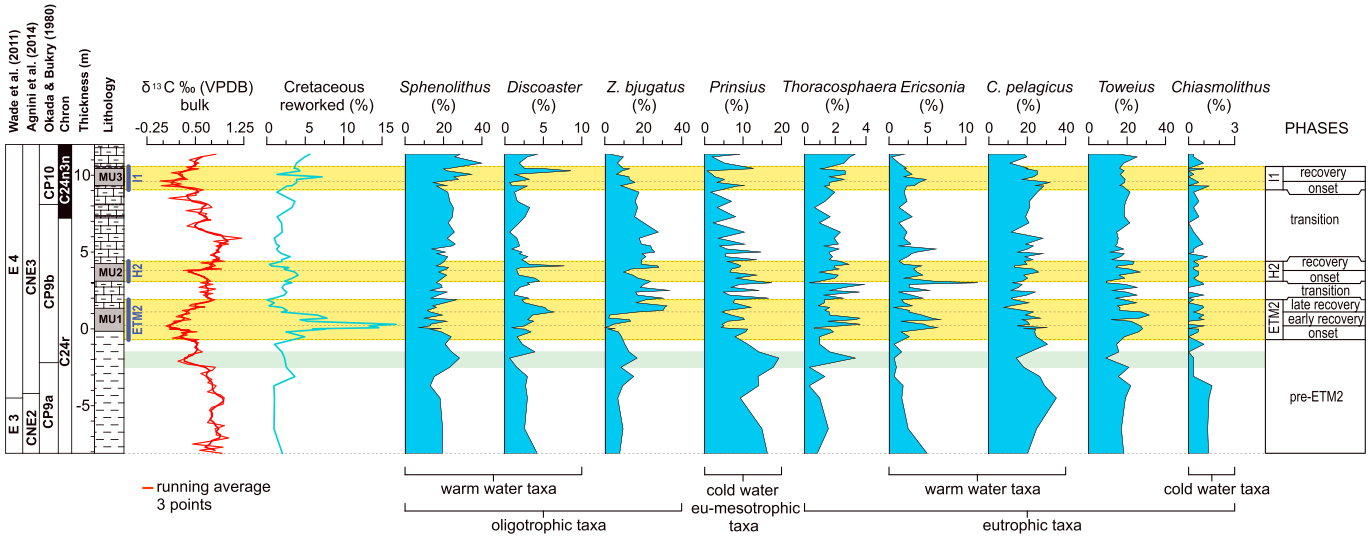

Figure 6. Changes in relative abundance of selected calcareous nannofossil genera and species across the studied segment of the Terche section, plotted against carbon stable isotope curve, biomagnetostratigraphy, and percentage of reworked Cretaceous nannofossil taxa. The yellow bands highlight the ETM2, H2, and I1 intervals as expressed by the $\delta^{13}C$ negative shifts. We identify 10 phases on the basis of the $\delta^{13}C$ curve variations (see Figure 4 and discussion in the text). The light green band underlines a minimum in carbon stable isotopes (see discussion in the text). For lithological symbols see Figure 2.

Zeauvigerina. Relatively higher values (12%) characterize the basal portion of the section, up to –4.70 m, and a slight increase (up to 15%) is recorded below the MU2. Variations of chiloguembelinids, though characterized by small percentages, mimic the changes in the subbotinid abundance. *Planorotalites*, *Globanomalina*, and *Pseudohastigerina* are very rare in the assemblages throughout the section. Each of them never exceeds the 3% in abundance and does not display significant variations within the MUs (Figure 5).

The benthic foraminiferal assemblage at the Terche section is strongly dominated by calcareous forms (~95% of the total). Preservation is generally good to moderate, and it improves within the marls cropping out between –8 and 0 m. Bolivinids are the most abundant forms throughout the studied interval, in particular, *Bolivinoides crenulata* (~30%) and smooth walled *Bolivina* (~20%), similarly to what is observed at the neighboring Farra, Alano, and Forada sections [*Agnini et al*., 2009; *Boscolo Galazzo et al*., 2013; *Giusberti et al*., 2016]. *Cibicides* spp. are also common at Terche (15–20%) and are the dominant epifaunals.

Radiolarians are generally scarcely represented at the Terche section (mean value around 2%), except for temporary increases observed across the MUs (Figure 5). Radiolarian peaks in abundance occur above the CIEs minima. Specifically, they reach the highest percentages within the MU1 (14.5%, +50 cm) and MU3 (17.9%, +9.73 m), while a minor peak (8.5%, +3.50 m) is recorded within the MU2 (Figure 5). In the studied interval, radiolarians are generally represented by taxa belonging to the spumellarians; however, also nassellarians occur within the MU1 and MU3.

4.6. Changes in Calcareous Nannofossil Assemblages

Within the segment B of the Terche section, the calcareous nannofossil assemblage is dominated by *Toweius*, *Coccolithus pelagicus*, and *Sphenolithus* (mean abundance of ~ 20% for each taxon). *Prinsius* and *Zygrhablithus* account for the 8% and 15%, respectively. The genera *Chiasmolithus*, *Discoaster*, *Ericsonia*, *Tribrachiatus*, and the calcareous dinocyst *Thoracosphaera* are minor components with an overall average abundance of ~ 8% (Figure 6 and Table S6).

Calcareous nannofossil assemblages show four major transient and striking modifications that are constrained by the main negative $\delta^{13}C$ shift (Figure 6). The lowest change is observed in coincidence to the negative $\delta^{13}C$ shift at –2.10 m. Specifically, a significant increase of *Prinsius*, *Sphenolithus*, *Zygrhablithus bijugatus*, and *Thoracosphaera* occurs along with a drop of *Discoaster*, *Ericsonia*, *Toweius*, and *Coccolithus pelagicus* (Figure 6). Across the three MUs are recorded the other marked modifications. These include an increase in the relative abundance of Cretaceous reworked taxa that is particularly marked at the MU1 (up to 17%). The distribution pattern of reworked forms mirrors the profile of the $CaCO_3$% and $\delta^{13}C$ curves (Figure 6). Concomitantly with the peaks in Cretaceous specimens, the taxa considered as oligotrophic, such as

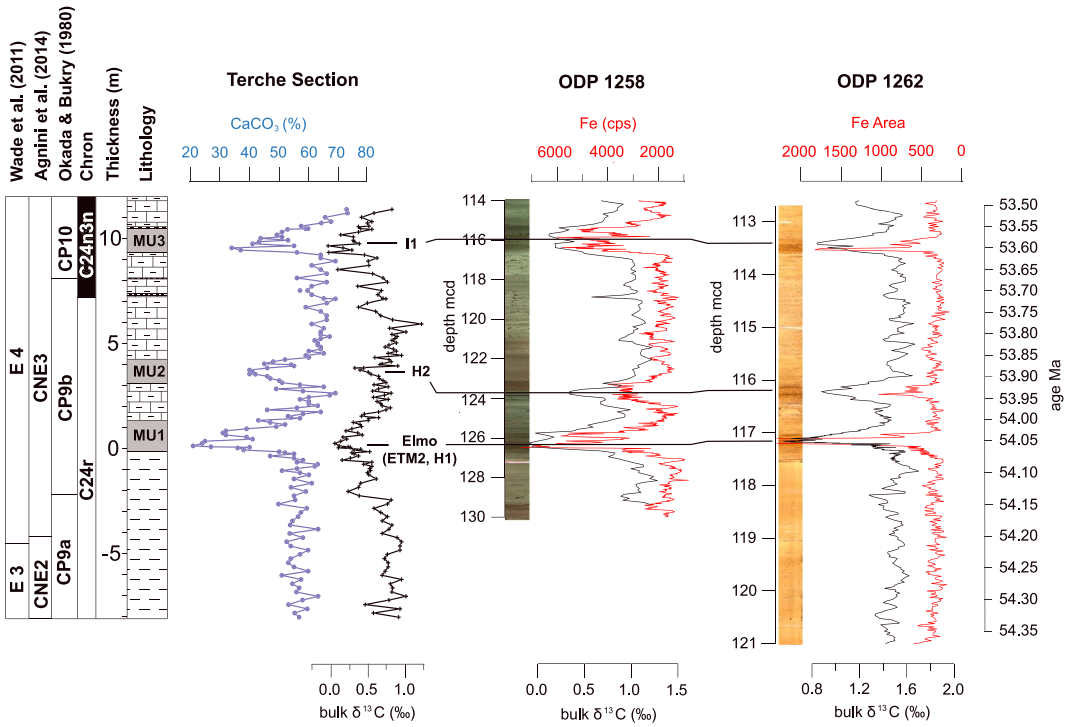

Figure 7. Correlation of the Terche section record to the ODP Site 1258 and 1262. From left to right, Terche section lithology with calcareous plankton biozonation and magnetostratigraphy; carbonate and stable carbon isotope data. For both Sites 1258 and 1262 bulk stable carbon isotope data (black line from *Zachos et al.* [2010], *Littler et al.* [2014], *Kirtland-Turner et al.* [2014], and *Westerhold et al.* [2012]), XRF core scanning Iron (Fe) intensity [*Westerhold and Röhl*, 2009; *Littler et al.*, 2014], and the core images are plotted versus depth. The age model for Site 1258 and 1262 [*Westerhold et al.*, 2015] is shown in the *y* axis on the very right; for reference the age model is given in Table 2b.

Discoaster, *Sphenolithus*, and *Z. bjiugatus* [e.g., *Wei and Wise*, 1990; *Gibbs et al.*, 2004, 2006; *Dunkley Jones et al.*, 2008; *Kahn and Aubry*, 2004; *Tremolada and Bralower*, 2004; *Villa et al.*, 2008; *Agnini et al.*, 2006, 2007a, 2009], decrease their abundance (Figure 6). In parallel, the genera *Thoracosphaera*, *Ericsonia*, *Toweius*, and, subordinately, the species *C. pelagicus* increase significantly their percentage. These latter forms are known as meso/eutrophic indices [e.g., *Perch-Nielsen*, 1981; *Fornaciari et al.*, 2007; *Agnini et al.*, 2006, 2007a, 2009; *Dedert et al.*, 2012; *Tremolada and Bralower*, 2004]. The oligotrophic *Discoaster* and *Zygrhablithus bijugatus* display a marked recovery in abundance in the upper MUs, with the exception of MU3 for *Z. bijugatus*. The genus *Prinsius* shows a slight general decrease throughout. *Sphenolithus* records minor changes throughout the section and displays a marked decline in abundance only within the MU1 (Figure 6).

5. Discussion

5.1. Stable Isotopes at the Terche Section: Reliability and Stratigraphy

The carbon isotope signal shows general trends very similar to those previously recorded by coeval bulk $\delta^{13}C$ profiles [e.g., *Cramer et al.*, 2003; *Lourens et al.*, 2005; *Nicolo et al.*, 2007; *Stap et al.*, 2009, 2010a; *Galeotti et al.*, 2010]. This is a robust indication that the carbon isotope signature has not been considerably affected by meteoric or burial diagenesis [e.g., *Marshall*, 1992; *Frank et al.*, 1999]. Our biomagnetostratigraphic data allow us to correlate the negative CIEs associated with MU1, MU2, and MU3 to the three post-PETM events ETM2, H2, and I1. Note that the CIEs span stratigraphic intervals larger than the thickness of the MUs (Figure 4). Here we consider the base of the ETM2, H2, and I1 events as coinciding with the onset of the respective negative $\delta^{13}C$ shifts. Similarly, the top of the events is related to the levels where the $\delta^{13}C$ profile returns to the pre-excursion values (Figure 4).

The absolute size of the ETM2 $\delta^{13}C$ negative shift is lower if compared to literature data [*Cramer et al.*, 2003; *Lourens et al.*, 2005; *Nicolo et al.*, 2007; *Stap et al.*, 2009, 2010a; *Galeotti et al.*, 2010]. We hypothesize that the

Table 2a. Depth Tie Points Terche Section to ODP 1258

Terche Section Level (m)	ODP 1258 Depth (rmcd)
−10.90	136.42
−8.22	133.96
−5.44	131.40
−0.87	127.10
0.18	126.38
0.72	125.86
2.56	124.38
4.51	122.66
9.50	116.31
9.78	115.91
10.57	115.07
11.37	114.22

original $\delta^{13}C$ signal was partially biased in our section by the huge input of reworked Cretaceous calcareous nannofossils (~17%), which presumably subdued the bulk sediment amplitude of the ETM2 CIE, and in a minor way, of the I1 CIE. A similar situation has been observed in the nearby Forada section where the CIE of the PETM is ~ 0.5‰ higher than other marine bulk carbonates [*Giusberti et al*., 2007]. The interpretation of the bulk carbonate isotope data may also be compromised by variations in diagenetic alteration among lithologic levels. However, the $\delta^{13}C$ versus $\delta^{18}O$ cross plot (Figure S4) displays a low correlation ($R^2 = 0.014$) between the two signals. This supports the hypothesis of a conservative behavior of the carbon isotope values in the studied samples that we consider as mainly reflecting changes in the isotopic composition of global oceanic carbon reservoir [e.g., *Marshall*, 1992].

Differently from the $\delta^{13}C$ curve, the $\delta^{18}O$ general profile is not consistent with the early Eocene oxygen isotope curves. Absolute $\delta^{18}O$ values, which scatter between −6.97‰ and −0.79‰ (Table S3), appear depleted by ~1‰ to 7‰ relatively to diagenetically unaltered marine calcite [e.g., *Zachos et al*., 2008]. This offset can be explained as reflecting elevated temperatures during lithification that usually enrich the isotopic composition in ^{16}O. Actually, when diagenetic processes occur well below the seafloor, where temperatures can exceed those of surface water, the $\delta^{18}O$ values of indurated limestones and marly limestone are significantly depleted in ^{18}O. Meteoric water might also have impacted our $\delta^{18}O$ record since rainwater generally has a $\delta^{18}O$ composition less than that of seawater [e.g., *Marshall*, 1992; *Schrag et al*., 1995; *Frank et al*., 1999].

5.2. Correlation to ODP Sites 1258 and 1262

After clear identification of the events ETM2, H2, and I1 by biomagnetostratigraphy the Terche section is correlated to the deep-sea reference records of ODP Site 1258 (Demerara Rise) and Site 1262 (Walvis Ridge), both South Atlantic. From these sites high-resolution XRF, isotopic records, and biomagnetostratigraphies are available for interbasinal correlations of the negative CIEs [*Suganuma and Ogg*, 2006; *Agnini et al*., 2007; *Westerhold et al*., 2007; *Westerhold and Röhl*, 2009; *Zachos et al*., 2010; *Kirtland-Turner et al*., 2014; *Littler et al*., 2014]. Correlation between ODP 1258 and Terche section is straightforward using the inverse XRF core scanning Fe intensity record and the $CaCO_3$ data (Figure 7). The ETM2 event even shows the two prominent peaks with the first one having higher amplitude then the second peak. Tables 2a and 2b give the age-depth tie points for the correlation. Based on the depth correlation, the most up to date age model for the interval in ODP Sites 1258 and 1262 [*Westerhold et al*., 2015] can be transferred to the Terche section and enables to compare data on a global scale.

5.3. Paleodepth of the Terche Section

The values recorded by the *P/B* at the Terche section are greater than 90% throughout (Figure 4). According to *Van der Zwaan et al*. [1990], these data suggest an average water depth of at least 1000 m. The common occurrence of *Nuttallides truempyi* and of deep-water agglutinants such as *Glomospira charoides*, *Karrerulina*

Table 2b. Age Tie Points ODP 1258

ODP 1258 Depth (rmcd)	Age La2011	405 kyr Cycle ID	Source (Reference)
91.50	52.412	Ec 9	*Westerhold et al*. [2008] and *Westerhold and Röhl* [2009]
99.00	52.820	Ec 8	*Westerhold et al*. [2008] and *Westerhold and Röhl* [2009]
107.00	53.216	Ec 7	*Westerhold et al*. [2008] and *Westerhold and Röhl* [2009]
116.00	53.612	Ec 6	*Westerhold et al*. [2008] and *Westerhold and Röhl* [2009]
126.00	54.012	Ec 5	*Westerhold et al*. [2008] and *Westerhold and Röhl* [2009]
139.90	54.424	Ec 4	*Westerhold et al*. [2008] and *Westerhold and Röhl* [2009]

spp., *Saccammina* spp., (upper depth limit at 300–500 m) [*van Morkhoven et al*., 1986; *Speijer and Schmitz*, 1998; *Kaminski and Gradstein*, 2005], and the common to rare occurrence of abyssal species such as *Clinapertina complanata*, *C. subplanispira*, and *Quadrimorphina profunda* [*Tjalsma and Lohmann*, 1983] confirm a fully bathyal paleodepth (1000–1500 m) [*van Morkhoven et al*., 1986] for the entire Terche section. The occurrence of abundant cibicidids does not contrast with this interpretation, as these forms presently can live up to abyssal depths [e.g., *Murray*, 1991, 2006]. The abundance of bolivinids in the study section is not related to the depositional depth, but it is a peculiar character of the successions deposited within the Belluno Basin. Specifically, this feature has been interpreted as an effect of lateral inputs of organic matter from the vicinity of lands and continental margins [*Boscolo Galazzo et al*., 2013; *Giusberti et al*., 2016].

5.4. Calcareous Plankton Preservation, Carbonate Dissolution, and Terrigenous Dilution Linked to Enhanced Hydrological Cycle

The three foraminiferal dissolution proxies (*F* index, WPCF, and *P*/*B*; Figure 4 and Table S4) adopted in our section ensure that the observed planktic foraminiferal changes mainly reflect responses to environmental modifications, even within the MUs, where the low $CaCO_3$% might suggest severe carbonate dissolution. Specifically, the *F* index shows distinct lower values in correspondence to the MUs with respect to those observed in nearby sections of the Belluno Basin across the PETM and K/X event [*Luciani et al*., 2007; *Agnini et al*., 2009]. The *P*/*B* index does not display any significant variation throughout the section, clearly indicating that there is no preferential dissolution of planktic tests with respect to the benthic shells. The WPCF shows as well minimum changes throughout the studied section.

Based on our outcomes we can reasonably consider changes in calcareous nannoplankton assemblages as largely reflecting variations in paleoenvironmental conditions of the photic zone. All the adopted proxies for calcareous nannofossils point to a general scarce influence of dissolution and overgrowth. In the entire Terche section the specific diversity, the $T_{species}$ and *T*/*D* are constantly high (Figure 4) even where dissolution is supposed to be present (the MUs). We attribute the minor decrease of $T_{species}$ and *T*/*D* values within the I1 recovery phase to a moderate increase in overgrowth rather than in carbonate dissolution. This is evident by a comparison with the Q_E and Q_O profiles (Figure 4).

The aforementioned evidences allow us to interpret the MUs deposition as mainly related to dilution rather than increase in dissolution. According to our age model (Figure 7), a distinct increase of the sedimentation rates occurred indeed across the investigated events. We infer the enhanced influence of terrigenous dilution within the MUs also by the associated Cretaceous reworking pulses (Figure 6). A significant input of reworked Cretaceous nannofossils is a feature shared by Eocene hyperthermals and the middle Eocene Climatic Optimum (MECO) in the Belluno Basin [*Agnini et al*., 2007a, 2009; *Toffanin et al*., 2011], an area influenced by a continental regime [e.g., *Giusberti et al*., 2007; *Boscolo Galazzo et al*., 2013]. The reworking has been linked to enhanced discharge of terrigenous material to the ocean, as derived from strengthened hydrological cycle. A significant increase in Cretaceous reworked specimens may hence relate to transient enrichments in nutrients washed off from lands [*Agnini et al*., 2009]. In the New Zealand slope marly beds coinciding with late Paleocene to early Eocene hyperthermals were interpreted by *Nicolo et al*. [2007] and *Slotnick et al*. [2012] as well as an effect of increased continental weathering and accelerated hydrological cycle.

Sedimentation rate and the Cretaceous reworking at Terche are considerably higher at the ETM2 with respect to H2 and I1. Therefore, the most significant perturbation of the hydrological cycle was linked to the climatic changes triggered by the ETM2.

5.5. Paleoenvironmental Scenarios Across the ETM2, H2, and I1 at the Terche Section

We reconstruct below the paleoenvironmental changes that occurred across the ETM2, H2, and I1 events using the calcareous plankton variations recorded at the Terche section, assuming that the dissolution proxies exclude significant taphonomic bias as discussed above (Figures 5 and 6).

The inferred interpretations are based on the known paleoecological affinities of planktic foraminifera and calcareous nannofossils, widely investigated in the past decades. There is indeed a general consensus that a number of calcareous nannofossil and planktic foraminiferal taxa are deeply sensitive to environmental variations reflecting climatic and oceanographic changes [e.g., *Okada and Honjo*, 1973; *Gibbs et al*., 2006; *Villa et al*., 2008; *Kalb and Bralower*, 2012; *Berggren et al*., 1978; *Boersma et al*., 1987; *Premoli Silva and Boersma*, 1988, 1989;

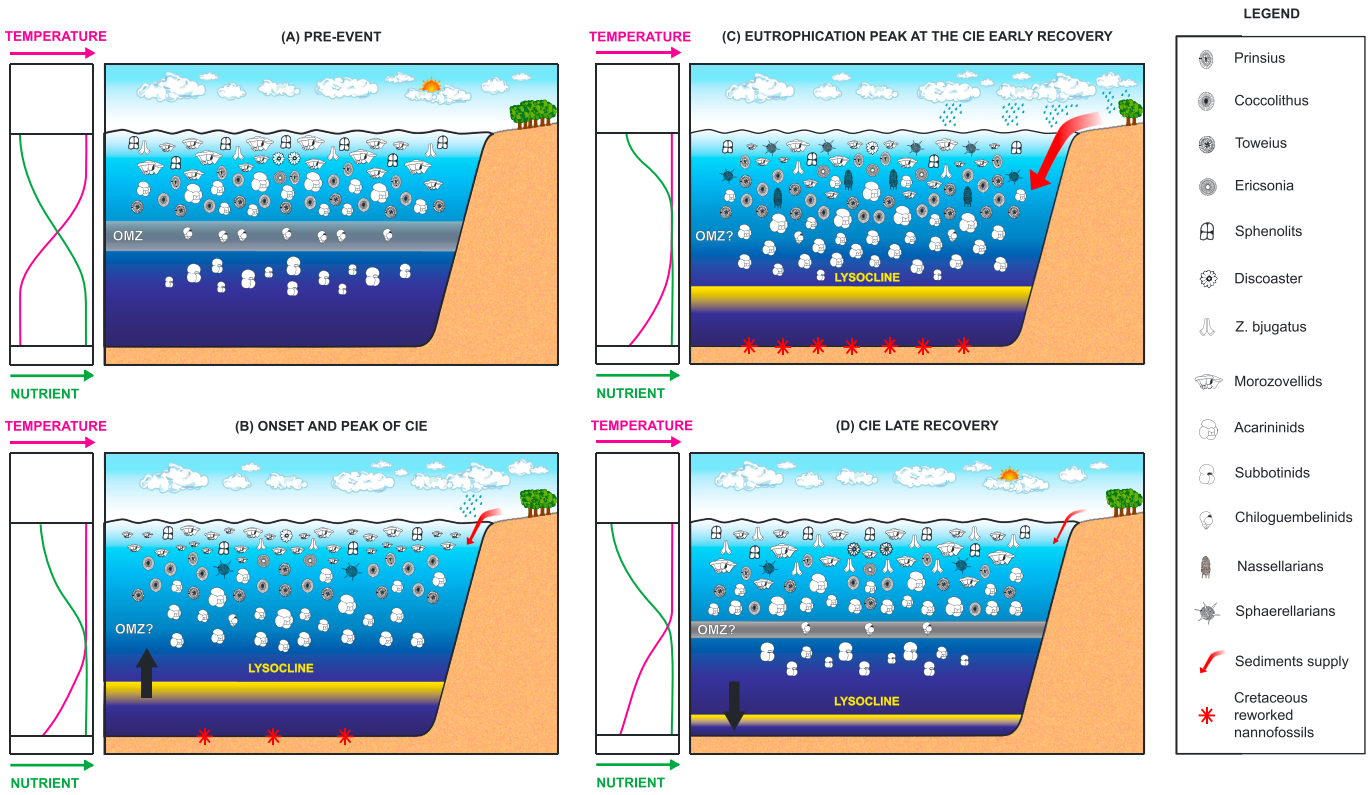

Figure 8. Cartoons illustrating the environmental scenarios across the ETM2 at the Tehyan Terche section deriving from the integrated record of changes in calcareous plankton and abiotic proxies. Similar sequences of environmental reconstructions, though less extreme, can be outlined for the H2 and I1 events (see more extensive discussions in the text). Depth is not in scale. (a) Pre-event: relatively warm, stable, and meso-oligotrophic conditions in the photic zone and structured water column with a relatively expanded OMZ. These conditions are similar to those observed during the ETM2-H2 and H2-I1 transition phases. (b) Onset and peak of the CIE: meso-eutrophic surface-water related to enhanced nutrient discharge induced by improved hydrological cycle coupled with collapse of thermal water-column stratification. (c) CIE early recovery: peak of eutrophic conditions relatively to the pre-event conditions in warm surface-water and still persistent weakening of thermal water-column stratification. (d) CIE late recovery: resume of relatively stable meso-oligotrophic environment in surface waters and of a stratified water column.

Pearson et al., 2006]. However, the role of environmental factors (e.g., temperature versus nutrient supply) on the fluctuations in Cenozoic calcareous plankton assemblages is not yet fully disentangled [e.g., *Agnini et al.*, 2007a, 2009; *Toffanin et al.*, 2011]. It is worth to point out that we lack of the independent $\delta^{18}O$ temperature proxy at Terche (see section 5.1). Therefore, our interpretation on changes in water temperatures is indirect and entirely based on modifications in the calcareous plankton assemblages.

5.5.1. Pre-ETM2 Relatively Stable and Oligotrophic Environment

During the interval preceding the ETM2 onset, planktic foraminifera were dominated by warm surface-dweller morozovellids and acarininids with moderate percentages of cold thermocline-dweller subbotinids (Figure 5). These features suggest a stable, thermally stratified water column, with a warm, oligotrophic surface layer and deeper cooler water rich in dissolved nutrient. The relatively common occurrence of low-oxygen tolerant chiloguembelinids [e.g., *Boersma et al.*, 1987; *Boersma and Premoli Silva*, 1989] supports the existence of a stratified water column with a moderately expanded oxygen minimum zone (OMZ) (Figure 8a). The sporadic occurrence of radiolarians, considered as eutrophy indicators [e.g., *Hallock*, 1987], confirms oligo-mesotrophic conditions at the surface waters. Nannofossils assemblages, during the pre-ETM2 interval, are well balanced in terms of average abundances of eutrophic (total of 55%) and oligotrophic (total of 45%) groups (Figure 6), indicating evenly distributed nutrients within the euphotic zone and no input excess.

The calcareous nannofossil assemblage shows a distinct short-lived ecological turnover coinciding with the pre-ETM2 minor negative CIE identified at ~ −2.10 m. Specifically, the cold-water index *Prinsius* and taxa with meso-oligotrophic affinities (*Sphenolitus* and *Z. bijugatus*) increase, while eutrophic taxa, such as *Ericsonia*, *Towieus*, and *Coccolithus* (with the only exception of *Thoracosphaera*) and the warm water index *Discoaster* drop (Figure 6). These data suggest that the pre-ETM2 CIE was probably associated with a cooling and/or

meso-oligotrophic episode. Planktic foraminifera do not display variations across this interval, possibly because this group was more sensitive to warming rather than cooling of the upper water column. A similar pre-ETM2 carbon-isotope feature has been recorded by *Stap et al*. [2009, 2010b] at ODP Site 1265 (Walvis Ridge). The pre-ETM2 $\delta^{13}C$ negative shift precedes at Terche the ETM2 minimum of circa 60 kyr. A comparable time interval can be estimated at Site 1265 [*Stap et al*., 2009, 2010b] between the ETM2 carbon isotope minimum and a positive peak in *Acarinina* $\delta^{18}O$ values that suggest a surface-water cooling episode preceding the ETM2. Colder temperatures just preceding the onset of the ETM2 are also reported in the Arctic Ocean (Lomonosov Ridge) by *Krishnan et al*. [2014].

All the adopted dissolution proxies (Figure 4) point to a depositional environment above the lysocline during the interval preceding the ETM2 onset.

5.5.2. Environmental Changes at the ETM2, H2, and I1 Events

Coinciding with the CIEs, calcareous plankton records at Terche prominent change in the assemblage composition (Figures 5 and 6). Such changes mainly reflect trends toward warmer and eutrophic conditions. The biotic and abiotic responses to the ETM2 largely replicate at the H2 and I1. Our results highlight, however, less intense perturbations across the H2, while the strongest disruption was at the ETM2. The amplitude of the biotic and environmental variations appears therefore somewhat proportional to the intensity of the carbon cycle perturbation as it has been documented globally.

5.5.2.1. Warming and Nutrient Enrichment in the Surface Waters at the CIE Onsets and Following Recoveries

In the Terche section, the acarininids marked increase across the ETM2, H2, and I1 CIEs indicates that each of these events was associated with a rise in surface water temperature in the central western Tethys, since this group inhabited the warm surface layer of the Eocene oceans.

The greatest abundance of Cretaceous nannofossil reworking, sign of transient enrichments in nutrients washed off from lands, occurred across the CIE onsets (Figures 6 and 8b) and ETM2 early recovery (Figure 8c), and it coincides with nannofossil eutrophic taxa maxima (*Ericsonia*, *Towieus*, and *Coccolithus*). On the contrary, taxa with oligotrophic affinities, precisely *Z. bijugatus* and even the warm-oligotrophic *Discoaster*, drop within the same intervals. Similar features were observed across the PETM and other hyperthermals in the Belluno Basin [e.g., *Agnini et al*., 2007a, 2009]. The increased input in radiolarians at the ETM2 early recovery and at the I1 recovery phases further supports a nutrient-rich surface waters environment.

Sphenoliths, thought to be adapted to oligotrophic warm-water conditions [e.g., *Young*, 1994; *Aubry*, 1998], do not show important changes except for a slight decrease at the ETM2 CIE onset. This suggests that sphenoliths were more influenced by trophic conditions than temperature in agreement with *Agnini et al*. [2007a] and *Toffanin et al*. [2011]. The lack of a clear sphenoliths response to the H2 and I1 can be explained with the minor magnitude of these events, which led to environmental perturbations below the threshold of sphenoliths sensitivity.

The combined results from calcareous nannofossils and planktic foraminifera point to an increase in surface-water eutrophication with respect to the pre-events conditions coupled with marked warmth at the CIE onsets and early recovery phases. The surface-dweller warm-index morozovellids, which largely shared the uppermost water-column habitat with acarininids [e.g., *Pearson et al*., 2006], show minor changes across the events consisting in transient declines in abundance (Figure 5). Surface-water nutrient enrichment along with weak water-column stratification is known to provide hostile ecological conditions for the highly specialized oligotrophic morozovellids [*Boersma et al*., 1987; *Pearson et al*., 2006; *Premoli Silva and Boersma*, 1989]. Slight differences between the paleoecology of morozovellids and acarininids are known by minor variations in stable isotopes that generally indicate a shallower habitat for the former [*Boersma et al*., 1979; *Pearson et al*., 1993; 2006].

The variations, though not particularly marked, of four of the adopted dissolution proxies (*F* index, WPCF, diversity, and Q_E) imply that the lysocline may have intercepted to some extent the depositional environment of the Terche section during these phases (Figures 8b and 8c).

Calcareous nannofossils suggest return to oligo-mesotrophic conditions within the photic zone only at the ETM2 CIE late recovery, and at the H2 and I1 recovery, where the Cretaceous reworking decreases implying a drop in terrigenous and nutrient supplies. The progressive reduction in radiolarian abundances, the recovery in oligotrophic indices (*Z. bjugatus*, *Discoaster* at ETM2 and H2; *Discoaster* at I1) and parallel decrease in eutrophic indicators toward the pre-event mean values (Figures 6 and 8d) confirm the restoration of

oligomesotrophy. Our record suggests that the major controlling factor driving *Discoaster* changes in abundance across the studied events was the excess in nutrient availability. Changes in temperature played a major role only when environmental conditions were meso-oligotrophic, as observed during the pre-ETM2 cooling episode where the drop of this genus is not paralleled by increase in Cretaceous reworked taxa, here adopted as proxy of enhanced nutrient availability. *Discoaster* displays actually low abundance when conditions became eutrophic and warmer and increases only when less eutrophic conditions coexisted with presumably still high temperatures, such as at ETM2 CIE late recovery, H2, and I1 recovery (Figure 6). The dominance of warm-water indicators among planktic foraminifera, mainly acarininids, across these phases suggests indeed still warm surface-water conditions.

5.5.2.2. Weakening of the Thermal Water-Column Stratification

The switch in abundance between acarininids and subbotinids recorded at the CIE onsets and early recoveries may reflect the onset of a significant warming of sub-surface layer besides the ocean-surface warmth. The pronounced increase in temperature related to the studied events may have caused a regional reduction of the thermal stratification making the subsurface waters unsuitable for deeper dwellers cold-index subbotinids (Figure 8b). These conditions favored the acarininids which might have been able to temporarily colonize warmer deep-waters previously occupied by subbotinids. The reduction in abundance of the chiloguembelinids within the whole CIE intervals (Figure 5) might support warming of sub-surface waters since this group thrived at the cool mid-high latitudes [e.g., *Boersma et al*., 1987]. On the other hand, chiloguembelinids are known to proliferate within OMZs [e.g., *Boersma et al*., 1987; *Boersma and Premoli Silva*, 1989], thus their reduction partly conflicts with our evidence of surface-water eutrophication that should in contrast induce an expansion of the OMZ. Altenatively, the thin-walled chiloguembelinids could have been partly lost during a rise of the lysocline. The rare chiloguembelinid fragments observed in coincidence to the F-index highest values, do not allow us to exclude that some of them may have been completely dissolved. The biserial chiloguembelinids can be considered among the most dissolution prone taxa as they have a thin-walled test and small size. Those features are considered as the most important factor controlling planktic foraminiferal dissolution [*Nguyen et al*., 2011]. Moreover, experiments on benthic foraminifera highlight that taxa with biserial architecture are more fragile than trochospirals [*Nguyen and Speijer*, 2014].

A partial replacement of the pre-events water-column structures occurred during the late recovery phases as indicated by the initial resuming in thermocline-dweller subbotinid and chiloguembelinid abundance (Figures 6 and 8d).

5.5.2.3. Reduced Size of Morozovellids at the ETM2 Onset

The morozovellid peak at the ETM2 onset is associated with significant reduction in their test size that involves, though at a lesser extent, also the acarininids. The morozovellid peak slightly precedes the eutrophication acme coinciding with the peak of nannofossil reworking and the highest radiolarian abundance (Figures 5 and 6). We speculate that the occurrence of relatively small morozovellids, coupled with a pronounced increase in abundance, is the combined results of stressors such as extreme warmth and increased eutrophication. The first phase of warming may have favored morozovellids until surface waters became exceedingly eutrophic for this group.

In the Holocene sediments size patterns are highly correlated with surface-water stratification, seasonality, and primary productivity on a regional scale [*Schmidt et al*., 2004]. A negative effect of fertility on size is suggested by the distinctly smaller size of the upwelling Holocene assemblages [*Schmidt et al*., 2004]. It is known that dwarfing in microfossils relates to extreme environmental stressors during biotic crisis or mass extinctions, even though it has been also observed as preceding the extinction level for some planktic foraminiferal species [e.g., *Wade and Olsson*, 2009; *Keller and Abramovich*, 2009]. Causes explaining the reduced size in fossil organisms are manifold, and they may include a collapse in primary production, a loss of symbiotic relationship, changes in salinity and temperature, and decrease in oxygen levels [e.g., *Hallam*, 1965; *Wade et al*., 2008]. It appears therefore that several different environmental, climatic, and ecological triggers may result in the same phenotypic response and it is problematic to determine precisely which factor is the main responsible for the transient dwarfing in the study case. We outline below a number of possible scenarios. Protists, both autotrophs and heterotrophs, reduce their cell size linearly with temperature [*Atkinson et al*., 2003], although direct laboratory tests on modern planktic foraminifera are lacking. The adaptation to reduce sinking rate within less dense warmer waters is one of the proposed causes invoked to explain the inverse temperature-size relationship for planktic protists [*Atkinson*, 1994]. The metabolism of protists accelerates

when temperature increases [e.g., *O'Connor et al*., 2009] thus requiring more resources, such as more oxygen. Since, in contrast, concentration of dissolved oxygen decreases in warm waters, a strategy to optimize resource uptake is to enlarge the ratio of surface area by reducing the cell mass [*Atkinson et al*., 2003]. Enhanced planktic foraminiferal metabolic rates have been proposed to explain the decrease in planktic foraminiferal productivity across another interval of intense warmth, the MECO at the Atlantic Site 1263 [*Boscolo Galazzo et al*., 2014]. The reduced sizes of morozovellids tests can also be explained as a consequence of a transient episode of photosymbionts loss (bleaching). The algal-symbiotic relationship is considered one of the most successful strategies adopted by morozovellids and acarininids during the earliest Paleogene [*Norris*, 1996; *Quillévéré et al*., 2001]. A number of mechanisms considered to be responsible for bleaching are expected to have occurred at the ETM2, such as elevated sea surface temperatures, increased CO_2, lower sea-water pH, and changes in nutrient availability [e.g., *Douglas*, 2003; *Wade et al*., 2008]. An episode of bleaching caused by global warming has been documented to explain the reduction in size of morozovelloidids and acarininds across the MECO [*Edgar et al*., 2012]. We cannot exclude the possibility that the loss of symbionts could have been the strategy adopted by morozovellids to temporarily adapt to eu-mesotrophic environments or to colonize relatively deeper habitats. Maximum size is normally achieved by planktic foraminifera within their preferred water mass, and it decreases away from such optimum environmental conditions [e.g., *Schmidt et al*., 2006]. Growth rate of morozovellids may have been reduced under the stress deriving from temporarily inhabiting deeper or relatively more fertile waters.

5.5.3. ETM2-H2 and H2-I1 Transitions: Restoring of Relatively Stable and Meso-oligotrophic Environments

Across the ETM2-H2 and H2-I1 transitions, both radiolarians and reworked Cretaceous nannofossils are low in abundance, pointing to low rates of terrigenous nutrient supply (Figure 8a). Calcareous plankton assemblages gradually recover toward pre-event conditions. The marked and possibly cyclic fluctuations in calcareous nannofossil abundances, particularly evident at the ETM2-H2 transition, suggest, however, still unstable conditions within the photic zone (Figure 6). The substantial increase of nannofossil oligotrophic indices (sphenoliths and *Z. bijugatus*) points to a restoration of oligotrophic surface waters, while the increase of subbotinids to pre-ETM2 values suggests the upper water-column return to be well stratified (Figures 5 and 8a).

5.6. Time Lag Between the CIEs and Biotic-Paleoenvironmental Recoveries

The strongest surface-water eutrophication, relatively to the pre-event conditions, was reached just following the ETM2 $\delta^{13}C$ minimum, in the early recovery phase, as indicated by the greatest abundances in radiolarians, eutrophic calcareous nannofossils, and low values in oligotrophic indices, such as *Discoaster*, *Z. bijugatus* and *Morozovella* (Figures 5, 6, and 8c). According to our age model, these conditions persisted over the circa 13–16 kyr long $\delta^{13}C$ early recovery phase. During this interval deep-dweller indices are still scarce among planktic foraminifera, while warm indices dominate thus implying a persistent weakening of the water-column thermal stratification (Figure 8c). High rates of sedimentation and significant input in reworked Cretaceous nannofossils persisted during the ETM2 early recovery and I1 recovery phases, thus highlighting that the perturbation of the hydrological cycle was still strengthened. However, this delay is not observed at the H2 event.

We record therefore an offset between the rate of carbon cycle recovery and the rate of environmental and biotic restorations, which were somewhat slower. Even though it is beyond the aim of our work to provide models for the current scenario of anthropogenic CO_2 additions and related upcoming global climate change, our analysis can give insight on how marine biota and environments can react to rapid and drastic global warming. It appears clear that the immediately stopping of the massive anthropogenic release in greenhouse gases will be insufficient to instantly invert the disruption of marine biota and the strengthening of terrestrial hydrological cycle.

6. Summary and Conclusions

We provide a unique record that directly integrates changes in planktic foraminiferal and calcareous nannofossil assemblages across the post-PETM carbon cycle perturbations related to the ETM2, H2, and I1 at the central western Tethyan Terche section (northeastern Italy). Our study contributes to partially fill the gap of knowledge on the biotic response to the events following the PETM and characterizing the early Eocene

climate. Differently from several deep-oceanic sites, our record displays only minimal evidences of carbonate dissolution making our results particularly relevant. Our records reveal the following:

1. During the studied events the calcareous plankton assemblages experienced significant changes indicating abrupt and transient episodes of environmental perturbations. Increased acarininid abundance, paralleled by subbotinid decline, suggests that each of the three carbon cycle disruptions was associated with upper water-column warming. Surface and subsurface waters warming may have led the weakening of the upper water column thermal stratification. This may have been the cause of the temporary decline in subbotinids. Changes in nannofossils assemblages along with increased radiolarian abundance point to surface-water nutrient enrichments and increased eutrophication relatively to the pre-event conditions.
2. We interpret surface-water eutrophication as forced by strengthening of the hydrological cycle and enhanced weathering. The enhanced discharge of terrigenous material is testified by increased sedimentation rates within the MUs, especially the MU1, and by peaks of reworked Cretaceous nannofossils. These features are also shared by PETM, X/K, and MECO events in the nearby areas influenced by a continental regime.
3. Across the studied events, calcareous nannofossils proved to be generally more susceptible to changes in nutrient supply, as can be expected for autotrophs, while planktic foraminiferal changes appear to have been mostly driven by warming rather than cooling of the upper water column.
4. Our data give insights on similarities and differences among the ETM2, H2, and I1 events from a Tethyan perspective, considering that the last two events are not unanimously regarded as hyperthermals. Calcareous plankton reacted in a similar way during all the events, with the most marked changes recorded at the ETM2. The ETM2 also records the most intense acceleration of the hydrological cycle. We can therefore conclude that ETM2 was the most prominent event. Nevertheless, the perturbations related to H2 and I1 were able to affect calcareous plankton, in particular, planktic foraminifera, and to induce changes in regional climate and oceanography.
5. The biotic changes and environmental perturbation at the ETM2 persisted after the CIE peaks for circa 13–16 kyr, during the early CIE recovery phase. Therefore, the recovery rates were slower for the environment and biota than for the carbon cycle. This has important implications in view of the modern human-induced carbon cycle disruption.

Acknowledgments

Data supporting this paper are available as in Tables S1–S6 and Figures S1–S4 in the supporting information. Funding for this research was provided by MIUR/PRIN COFIN 2010–2011, coordinated by D. Rio. V.L. and R. D'O. were financially supported by FAR from the Ferrara University, and L.G., E.F., and F.B. G. received financial support from Padova University (Progetto di Ateneo GIUSPRAT10 CPDA 108242/10 and ex 60% E. Fornaciari). E.D. was financially supported by Deutsche Forschungsgemeinschaft (DFG) project number DA1757/1-1. The manuscript greatly benefited from constructive suggestions by two anonymous reviewers and Editor.

References

Abels, H. A., W. C. Clyde, P. D. Gingerich, F. J. Hilgen, H. C. Fricke, G. J. Bowen, and L. J. Lourens (2012), Terrestrial carbon isotope excursions and biotic change during Palaeogene hyperthermals, *Nat. Geosci.*, *5*(5), 326–329, doi:10.1038/ngeo1427.

Adelseck, C. G., Jr., G. W. Geehan, and P. H. Roth (1973), Experimental evidence for the selective dissolution and overgrowth of calcareous nannofossils during diagenesis, *Geol. Soc. Am. Bull.*, *84*(8), 2755–2762, doi:10.1130/0016-7606(1973)84.

Agnini, C., G. Muttoni, D. V. Kent, and D. Rio (2006), Eocene biostratigraphy and magnetic stratigraphy from Possagno, Italy: The calcareous nannofossil response to climate variability, *Earth Planet. Sci. Lett.*, *241*, 815–830, doi:10.1016/j.epsl.2005.11.005.

Agnini, C., E. Fornaciari, D. Rio, F. Tateo, J. Backman, and L. Giusberti (2007a), Responses of calcareous nannofossil assemblages, mineralogy and geochemistry to the environmental perturbations across the Paleocene/Eocene boundary in the Venetian pre-Alps, *Mar. Micropaleontol.*, *63*, 19–38, doi:10.1016/j.marmicro.2006.10.002.

Agnini, C., E. Fornaciari, I. Raffi, D. Rio, U. Röhl, and T. Westerhold (2007), High resolution nannofossil biochronology of middle Paleocene to early Eocene at ODP Site 1262: Implications for calcareous nannoplankton evolution, *Mar. Micropaleontol.*, *64*, 215–248, doi:10.1016/j.marmicro.2007.05.003.

Agnini, C., J. Backman, H. Brinkhuis, E. Fornaciari, L. Giusberti, V. Luciani, D. Rio, and A. Sluijs (2009), An early Eocene carbon cycle perturbation at similar to 52.5 Ma in the Southern Alps: Chronology and biotic response, *Paleoceanography*, *24*, PA2209, doi:10.1029/2008PA001649.

Agnini, C., E. Fornaciari, I. Raffi, R. Catanzariti, H. Pälike, J. Backman, and D. Rio (2014), Biozonation and biochronology of Paleogene calcareous nannofossils from low and middle latitudes, *Newslett. Stratigr.*, *47*(2), 131–181, doi:10.1127/0078-0421/2014/0042.

Agnini, C., D. J. A. Spofforth, G. R. Dickens, D. Rio, H. Pälike, J. Backman, G. Muttoni, and E. Dallanave (2016), Stable isotope and calcareous nannofossil assemblage records for the Cicogna section: Toward a detailed template of late Paleocene and early Eocene global carbon cycle and nannoplankton evolution, *Clim. Past*, *12*, 883–909, doi:10.5194/cp-12-883-2016.

Atkinson, D. (1994), Temperature and organism size—A biological law for ectotherms?, *Adv. Ecol. Res.*, *25*, 1–58.

Atkinson, D., B. J. Ciotti, and D. J. S. Montagnes (2003), Protists decrease in size linearly with temperature: Ca. 2.5%°C^{-1}, *Proc. R. Soc. Lond. B.*, *270*, 2605–2611, doi:10.1098/rspb.2003.2538.

Aubry, M.-P. (1998), Early Paleogene calcareous nannoplankton evolution: A tale of climatic amelioration, in *Late Paleocene and Early Eocene Climatic and Biotic Evolution*, edited by M.-P. Aubry et al., pp. 158–203, Columbia Univ. Press, New York.

Backman, J., and N. J. Shackleton (1983), Quantitative biochronology of Pliocene and early Pleistocene calcareous nannoplankton from the Atlantic, Indian and Pacific Oceans, *Mar. Micropaleontol.*, *8*, 141–170.

Bé, A. W. H., W. M. John, and M. H. Stanley (1975), Progressive dissolution and ultrastructural breakdown of planktic foraminifera, *Cushman Found. Foraminiferal Res. Spec. Publ.*, *13*, 27–55.

Berger, W. H. (1970), Planktonic foraminifera—Selective solution and lysocline, *Mar. Geol.*, *8*(2), 111–138.

Berger, W. H. (1973), Deep-sea carbonates: Pleistocene dissolution cycles, *J. Foraminiferal Res.*, *3*(4), 187–195.

Berger, W. H., M.-C. Bonneau, and F. L. Parker (1982), Foraminifera on the deep-sea floor: Lysocline and dissolution rate, *Oceanol. Acta*, *5*(2), 249–258.

Berggren, W. A., M. C. Mckenna, J. Hardenbol, and J. D. Obradovich (1978), Revised Paleogene polarity time scale, *J. Geol.*, *86*(1), 67–81.
Boersma, A., and I. Premoli Silva (1989), Atlantic paleogene biserial heterohelicid foraminifera and oxygen minima, *Paleoceanography*, *4*(3), 271–286, doi:10.1029/PA004i003p00271.
Boersma, A., N. J. Shackleton, M. A. Hall, and Q. C. Given (1979), Carbon and oxygen isotope variations at DSDP Site 384 (North Atlantic) and some paleotemperature and carbon isotope variations in the Atlantic Ocean, *Init. Repts. DSDP*, *43*, 695–717.
Boersma, A., I. Premoli Silva, and N. J. Shackleton (1987), Atlantic Eocene planktonic foraminiferal paleohydrographic indicators and stable isotope paleoceanography, *Paleoceanography*, *2*(3), 287–331, doi:10.1029/PA002i003p00287.
Bornemann, A., and J. Mutterlose (2008), Calcareous nannofossil and $\delta^{13}C$ records from the Early Cretaceous of the western Atlantic ocean: Evidence for enhanced fertilization across the Berriasian–Valanginian transition, *Palaios*, *23*(12), 821–832, doi:10.2110/palo.2007.p07-076r.
Boscolo Galazzo, F., L. Giusberti, V. Luciani, and E. Thomas (2013), Paleoenvironmental changes during the Middle Eocene Climatic Optimum (MECO) and its aftermath: The benthic foraminiferal record from the Alano section (NE Italy), *Palaeogeogr. Palaeoclimatol. Palaeoecol.*, *378*, 22–35, doi:10.1016/j.palaeo.2013.03.018.
Boscolo Galazzo, F., L. M. Pagani, C. Warren, X. E. Thomas, V. Luciani, and L. Giusberti (2014), The middle Eocene climatic optimum (MECO): A multiproxy record of paleoceanographic changes in the southeast Atlantic (ODP Site 1263, Walvis Ridge), *Paleoceanography*, *29*, 1143–1161, doi:10.1002/2014PA002670.
Bosellini, A. (1989), Dynamics of Tethyan carbonate platform, in *Controls on Carbonate Platform and Basin Platform*, *Soc. Sediment. Geol. (SEPM) Spec. Publ.*, vol. 44, edited by P. D. Crevello et al., pp. 3–13. Univ. of California, Berkeley.
Chew, A. E. (2015), Mammal faunal change in the zone of the Paleogene hyperthermals ETM2 and H2, *Clim. Past*, *11*, 1223–1237, doi:10.5194/cp-11-1223-2015.
Clementz, M., S. Bajpai, V. Ravikant, J. G. M. Thewissen, N. Saravanan, I. B. Singh, and V. Prasad (2011), Early Eocene warming events and the timing of terrestrial faunal exchange between India and Asia, *Geology*, *39*(1), 15–18, doi:10.1130/G31585.1.
Coccioni, R., G. Bancalà, R. Catanzariti, E. Fornaciari, F. Frontalini, L. Giusberti, L. Jovane, V. Luciani, J. Savian, and M. Sprovieri (2012), An integrated stratigraphic record of the Palaeocene-lower Eocene at Gubbio (Italy), New insights into the early Palaeogene hyperthermals and carbon isotope excursions, *Terra Nova*, *24*, 380–386, doi:10.1111/j.1365-3121.2012.01076.x.
Cramer, B. S., D. V. Kent, and M.-P. Aubry (2003), Orbital climate forcing of excursions in the late Paleocene–early Eocene (chrons C24n–C25n), *Paleoceanography*, *18*(4), 1097, doi:10.1029/2003PA000909.
D'haenens, S., A. Bornemann, P. Stassen, and R. P. Speijer (2012), Multiple early Eocene benthic foraminiferal assemblage and δ13C fluctuations at DSDP Site 401 (Bay of Biscay-NE Atlantic), *Mar. Micropaleontol.*, *88–89*, 15–35, doi:10.1016/j.marmicro.2012.02.006.
D'haenens, S., A. Bornemann, P. Claeys, U. Röhl, E. Steurbaut, and R. P. Speijer (2014), A transient deep-sea circulation switch during Eocene Thermal Maximum 2, *Paleoceanography*, *29*, 370–388, doi:10.1002/2013PA002567.
Dallanave, E., C. Agnini, G. Muttoni, and D. Rio (2009), Magneto-biostratigraphy of the Cicogna section (Italy): Implications for the late Paleocene–early Eocene time scale, *Earth Planet. Sci. Lett.*, *285*, 39–51.
Dallanave, E., L. Tauxe, G. Muttoni, and D. Rio (2010), Silicate weathering machine at work: Rock magnetic data from the late Paleocene-early Eocene Cicogna section, Italy, *Geochem. Geophys. Geosyst.*, *11*, Q07008, doi:10.1029/2010GC003142.
Dallanave, E., C. Agnini, G. Muttoni, and D. Rio (2012a), Paleocene magneto-biostratigraphy and climate-controlled rock magnetism from the Belluno Basin, Tethys Ocean, Italy, *Palaeogeogr. Palaeoclimatol. Palaeoecol.*, *337-338*, 130–142.
Dallanave, E., G. Muttoni, C. Agnini, L. Tauxe, and D. Rio (2012), Is there a normal magnetic-polarity event during the Palaeocene-Eocene thermal maximum (~55 Ma)? Insights from the palaeomagnetic record of the Belluno Basin (Italy), *Geophys. J. Int.*, *191*, 517–529.
De Conto, R. M., S. Galeotti, M. Pagani, D. Tracy, K. Schaefer, T. Zhang, D. Pollard, and D. J. Beerling (2012), Past extreme warming events linked to massive carbon release from thawing permafrost, *Nature*, *484*, 87–91, doi:10.1038/nature10929.
Dedert, M., H. M. Stoll, D. Kroon, N. Shimizu, K. Kanamaru, and P. Ziveri (2012), Productivity response of calcareous nannoplankton to Eocene Thermal Maximum 2 (ETM2), *Clim. Past*, *8*(3), 977–993, doi:10.5194/cp-8-977-2012.
Dedert, M., H. Stoll, S. Kars, J. R. Young, N. Shimizu, D. Kroon, L. Lourens, and P. Ziveri (2014), Temporally variable diagenetic overgrowth on deep-sea nannofossil carbonates across Palaeogene hyperthermals and implications for isotopic analyses, *Mar. Micropaleontol.*, *107*, 18–31.
Dickens, G. R. (2011), Down the rabbit hole: Toward appropriate discussion of methane release from gas hydrate systems during the Paleocene-Eocene thermal maximum and other past hyperthermal events, *Clim. Past*, *7*(3), 831–846, doi:10.5194/cp-7-831-2011.
Douglas, A. E. (2003), Coral bleaching—How and why?, *Mar. Pollut. Bull.*, *46*, 385–392.
Dunkley Jones, T., P. R. Bown, P. N. Pearson, B. S. Wade, H. K. Coxall, and C. H. Lear (2008), Major shifts in calcareous phytoplankton assemblages through the Eocene-Oligocene transition of Tanzania and their implications for low-latitude primary production, *Paleoceanography*, *23*, PA4204, doi:10.1029/2008PA001640.
Edgar, K. M., S. M. Bohaty, S. J. Gibbs, P. F. Sexton, R. D. Norris, and P. A. Wilson (2012), Symbiont "bleaching" in planktic foraminifera during the Middle Eocene Climatic Optimum, *Geology*, *41*, 15–18, doi:10.1130/G33388.1.
Fisher, R. (1953), Dispersion on a sphere, *Proc. R. Soc. London*, *217*, 295–305.
Fornaciari, E., L. Giusberti, V. Luciani, F. Tateo, C. Agnini, J. Backman, M. Oddone, and D. Rio (2007), An expanded Cretaceous – Tertiary transition in a pelagic setting of the Southern Alps (central-western Tethys), *Palaeogeor. Palaeoclimatol. Palaeoecol.*, *255*, 98–131, doi:10.1016/j.palaeo.2007.02.044.
Frank, T. D., M. A. Arthur, and W. E. Dean (1999), Diagenesis of Lower Cretaceous pelagic carbonates, North Atlantic: Paleoceanographic signals obscured, *J. Foraminiferal Res.*, *29*, 340–351.
Galeotti, S., S. Krishnan, M. Pagani, L. Lanci, A. Gaudio, J. C. Zachos, S. Monechi, G. Morelli, and L. J. Lourens (2010), Orbital chronology of Early Eocene hyperthermals from the Contessa Road section, central Italy, *Earth Planet. Sci. Lett.*, *290*(1–2), 192–200, doi:10.1016/j.epsl.2009.12.021.
Gardin, S., and S. Monechi (1998), Palaeoecological change in middle to low latitude calcareous nannoplankton at the Cretaceous/Tertiary boundary, *Bull. Soc. Geol. Fr.*, *169*(5), 709–723.
Gibbs, S. J., N. J. Shackleton, and J. R. Young (2004), Orbitally forced climate signals in mid-Pliocene nannofossil assemblages, *Mar. Micropaleontol.*, *51*, 39–56.
Gibbs, S. J., T. J. Bralower, P. R. Bown, J. C. Zachos, and L. M. Bybell (2006), Shelf and open ocean calcareous phytoplankton assemblages across the Paleocene–Eocene thermal maximum: Implications for global productivity gradients, *Geology*, *34*(4), 233–236.
Gibbs, S. J., P. R. Bown, B. H. Murphy, A. Sluijs, K. M. Edgar, H. Pälike, C. T. Bolton, and J. C. Zachos (2012), Scaled biotic disruption during early Eocene global warming events, *Biogeosciences*, *9*(11), 4679–4688, doi:10.5194/bg-9-4679-2012.
Giusberti, L., D. Rio, C. Agnini, J. Backman, E. Fornaciari, F. Tateo, and M. Oddone (2007), Mode and tempo of the Paleocene–Eocene thermal maximum in an expanded section from the Venetian pre-Alps, *Geol. Soc. Am. Bull.*, *119*, 391–412, doi:10.1130/B25994.1.

Giusberti, L., F. Boscolo Galazzo, and E. Thomas (2016), Variability in climate and productivity during the Paleocene/Eocene thermal maximum in the Central-Western Tethys (Forada section), *Clim. Past*, *12*, 1–28, doi:10.5194/cp-12-1-2016.
Hallam, A. (1965), Environmental causes of stunting in living and fossil marine benthonic invertebrates, *Palaeontology*, *8*, 132–155.
Hallock, P. (1987), Fluctuations in the trophic resource continuum: A factor in global diversity cycles?, *Paleoceanography*, *2*, 457–471, doi:10.1029/PA002i005p00457.
Hancock, H. J. L., and G. R. Dickens (2005), Carbonate dissolution episodes in Paleocene and Eocene sediment, Shatsky Rise, west-central Pacific, in *Proceedings of the Ocean Drilling Program, Scientific Results*, vol. 198, edited by T. J. Bralower, I. Premoli Silva, and M. J. Malone, 1-24, Texas A&M Univ., College Station. [Available at World Wide Web http://www-odp.tamu.edu/publications/198_SR/116/116.htm.]
Hollis, C. J., G. R. Dickens, B. D. Field, C. M. Jones, and C. P. Strong (2005), The Paleocene–Eocene transition at Mead Stream, New Zealand: A southern Pacific record of early Cenozoic global change, *Palaeogeogr. Palaeoclimatol. Palaeoecol.*, *215*(3), 313–343, doi:10.1016/j.palaeo.2004.09.011.
Hönisch, B., et al. (2012), The geological record of ocean acidification, *Science*, *335*, 1058–1063, doi:10.1126/science.1208277.
Höntzsch, S., C. Scheibner, E. Guasti, J. Kuss, A. M. Marzouk, and M. W. Rasser (2011), Increasing restriction of the Egyptian shelf during the early Eocene? New insights from a southern Tethyan carbonate platform, *Palaeogeogr. Palaeoclimatol. Palaeoecol.*, *302*(3), 349–366, doi:10.1016/j.palaeo.2011.01.022.
Jennions, S. M., E. Thomas, D. N. Schmidt, D. Lunt, and A. Ridgwell (2015), Changes in benthic ecosystems and ocean circulation in the Southeast Atlantic across Eocene Thermal Maximum 2, *Paleoceanography*, *30*, 1059–1077, doi:10.1002/2015PA002821.
Jones, C. H. (2002), User-driven integrated software lives: "Paleomag" paleomagnetics analysis on the Macintosh, *Comput. Geosci.*, *28*, 1145–1151.
Kahn, A., and M.-P. Aubry (2004), Provincialism associated with the Paleocene/Eocene thermal maximum: Temporal constraint, *Mar. Micropaleontol.*, *52*(1), 117–131, doi:10.1016/j.marmicro.2004.04.003.
Kalb, A. L., and T. J. Bralower (2012), Nannoplankton origination events and environmental changes in the late Paleocene and early Eocene, *Mar. Micropaleontol.*, *92–93*, 1–115.
Kaminski, M. A., and F. M. Gradstein (2005), in *Atlas of Paleogene Cosmopolitan Deep-water Agglutinated Foraminifera*, *Gryzbowski Foundation Spec. Publ.*, vol. 10, edited by M. A. Kaminski and F. M. Gradstein, pp. 547, Krakow, Poland.
Keller, G., and S. Abramovich (2009), Lilliput Effect in late Maastrichtian Planktic Foraminifera: Response to Environmental Stress, *Palaeogeogr. Palaeoclimatol. Palaeoecol.*, *284*, 47–62.
Kennett, J. P., and L. D. Stott (1991), Abrupt deep-sea warming, palaeoceanographic changes and benthic extinctions at the end of the Palaeocene, *Nature*, *353*, 225–229.
Kent, D. V., P. E. Olsen, and W. K. Witte (1995), Late Triassic-earliest Jurassic geomagnetic polarity sequence and paleolatitudes from drill cores in the Newark rift basin, eastern North America, *J. Geophys. Res.*, *100*, 14,965–14,998, doi:10.1029/95JB01054.
Kirschvink, J. L. (1980), The least-squares line and plane and the analysis of palaeomagnetic data, *Geophys. J. R. Astron. Soc.*, *62*, 699–718.
Kirtland-Turner, S., P. F. Sexton, C. D. Charles, and R. D. Norris (2014), Persistence of carbon release events through the peak of early Eocene global warmth, *Nat. Geosci.*, *12*, 1–17, doi:10.1038/ngeo2240.
Krishnan, S., M. Pagani, M. Huber, and A. Sluijs (2014), High latitude hydrological changes during the Eocene Thermal Maximum 2, *Earth Planet. Sci. Lett.*, *404*, 167–177, doi:10.1016/j.epsl.2014.07.029.
Lauretano, V., K. Littler, M. Polling, and J. C. Zachos (2015), Frequency, magnitude and character of hyperthermal events at the onset of the Early Eocene Climatic Optimum, *Clim. Past*, *11*(3), 1795–1820, doi:10.5194/cpd-11-1795-2015.
Leon-Rodriguez, L., and G. R. Dickens (2010), Constraints on ocean acidification associated with rapid and massive carbon injections: The early Paleogene record at ocean drilling program site 1215, equatorial Pacific Ocean, *Palaeogeogr. Palaeoclimatol. Palaeoecol.*, *298*(3–4), 409–420, doi:10.1016/j.palaeo.2010.10.029.
Lirer, F. (2000), A new technique for retrieving calcareous microfossils from lithified lime deposits, *Micropaleontology*, *46*, 365–369.
Littler, K., U. Röhl, T. Westerhold, and J. C. Zachos (2014), A high-resolution benthic stable isotope record for the South Atlantic: Implications for orbital-scale changes in late Paleocene–early Eocene climate and carbon cycling, *Earth Planet. Sc. Lett.*, *401*, 18–30, doi:10.1016/j.epsl.2014.05.054.
Lourens, L. J., A. Sluijs, D. Kroon, J. C. Zachos, E. Thomas, U. Röhl, J. Bowles, and I. Raffi (2005), Astronomical pacing of late Palaeocene to early Eocene global warming events, *Nature*, *435*, 1083–1087.
Lowrie, W., and W. Alvarez (1977), Upper Cretaceous magnetic stratigraphy, in *Upper Cretaceous–Paleocene Magnetic Stratigraphy at Gubbio, Italy*, *Geol. Soc. Am.*, vol. 88, edited by W. Lowrie, and W. Alvarez, 374–377, Geol. Soc. Am., Boulder, Colo., doi:10.1130/0016-7606.
Luciani, V., L. Giusberti, C. Agnini, J. Backman, E. Fornaciari, and D. Rio (2007), The Paleocene–Eocene Thermal Maximum as recorded by Tethyan planktonic foraminifera in the Forada section (northern Italy), *Mar. Micropaleontol.*, *64*(3), 189–214, doi:10.1016/j.marmicro.2007.05.001.
Luciani, V., G. R. Dickens, J. Backman, E. Fornaciari, L. Giusberti, C. Agnini, and R. D'Onofrio (2016), Major perturbations in the global carbon cycle and photosymbiont-bearing planktic foraminifera during the early Eocene, *Clim. Past*, *12*, 981–1007, doi:10.5194/cp-12-981-2016.
Lunt, D. J., A. Ridgwell, A. Sluijs, J. C. Zachos, S. Hunter, and A. Haywood (2011), A model for orbital pacing of methan hydrate destabilization during the Paleogene, *Nat. Geosci.*, *4*, 775–778, doi:10.1038/ngeo1266.
MacKenzie, D. T., III, and S. W. Wise Jr. (1983), Paleocene and Eocene calcareous nannofossils from Deep Sea Drilling Project Legs 25 and 40, south and east of Africa, in *Deep Sea Drilling Project, Initial Reports., 71*, edited by W. J. Ludwig et al., pp. 1141-1180, U.S. Gov. Print. Off., Washington, D. C., doi:10.2973/dsdp.proc.71.147.1983.
Marshall, J. D. (1992), Climatic and oceanographic isotopic signals from the carbonate rock record and their preservation, *Geol. Mag.*, *129*(02), 143–160.
Martini, E. (1971), Standard Tertiary and Quaternary calcareous nannoplankton zonation, in *Proceedings of the Second Planktonic Conference*, vol. 1970, edited by A. Farinacci, pp. 739–785, Tecnoscienza, Roma.
McInerney, F. A., and S. L. Wing (2011), The Paleocene-Eocene Thermal Maximum: A perturbation of carbon cycle, climate, and biosphere with implications for the future, *Annu. Rev. Earth Planet. Sci.*, *39*(1), 489–516, doi:10.1146/annurev-earth-040610-133431.
Murray, J. W. (1976), A method of determining proximity of marginal seas to an ocean, *Mar. Geol.*, *22*, 103–119.
Murray, J. W. (Ed.) (1991), *Ecology and Paleoecology of Benthic Foraminifera*, pp. 398, Longman Scientific and Technical, Harlow Essex, U. K.
Murray, J. W. (Ed.) (2006), *Ecology and Applications of Benthic Foraminifera*, pp. 426, Cambridge Univ. Press, New York.
Nguyen, T. M. P., and R. P. Speijer (2014), A new procedure to assess dissolution based on experiments on Pliocene–Quaternary foraminifera (ODP Leg 160, Eratosthenes Seamount, Eastern Mediterranean), *Mar. Micropaleontol.*, *106*, 22–39, doi:10.1016/j.marmicro.2013.11.004.

Nguyen, T. M. P., M.-R. Petrizzo, and R. P. Speijer (2009), Experimental dissolution of a fossil foraminiferal assemblage (Paleocene–Eocene Thermal Maximum, Dababiya, Egypt): Implications for paleoenvironmental reconstructions, *Mar. Micropaleontol.*, *73*(3–4), 241–258, doi:10.1016/j.marmicro.2009.10.005.

Nguyen, T. M. P., M.-R. Petrizzo, P. Stassen, and R. P. Speijer (2011), Dissolution susceptibility of Paleocene–Eocene planktic foraminifera: Implications for palaeoceanographic reconstructions, *Mar. Micropaleontol.*, *81*(1–2), 1–21.

Nicolo, M. J., G. R. Dickens, C. J. Hollis, and J. C. Zachos (2007), Multiple early Eocene hyperthermals: Their sedimentary expression on the New Zealand continental margin and in the deep sea, *Geology*, *35*(8), 699–702.

Norris, R. D. (1996), Symbiosis as an evolutionary innovation in the radiation of Paleocene planktic foraminifera, *Paleobiology*, *22*(4), 461–480.

O'Connor, M., M. F. Piehler, D. M. Leech, A. Anton, and J. F. Bruno (2009), Warming and resource availability shift food web structure and metabolism, *Plos Biol.*, *7*(8), 1–6, doi:10.1371/journal.pbio.1000178.

Okada, H., and D. Bukry (1980), Supplementary modification and introduction of code numbers to the low latitude coccolith biostratigraphy zonation (Bukry, 1973, 1975), *Mar. Micropaleontol.*, *51*, 321–325.

Okada, H., and S. Honjo (1973), The distribution of oceanic coccolithophorids in the Pacific, *Deep Sea Res. Oceanogr. Abstr.*, *20*(4), 355–374, doi:10.1016/0011-7471(73)90059-4.

Olsson, R. K., C. Hemleben, W. A. Berggren, and B. T. Huber (1999), *Atlas of Paleocene Planktonic Foraminifera*, *Smithsonian Contribution to Paleobiology*, vol. 85, pp. 225, Smithsonian Institution Press, Washington D. C.

Pagani, M., K. Caldeira, D. Archer, and J. C. Zachos (2006), An ancient carbon mystery, *Science*, *314*, 1556–57, doi:10.1126/science.1136110.

Pearson, P. N., N. J. Shackleton, and M. A. Hall (1993), Stable isotope paleoecology of middle Eocene planktonic foraminifera and multi-species isotope stratigraphy, DSDP Site 523, South Atlantic, *J. Foraminiferal Res.*, *23*, 123-140, doi:10.2113/gsjfr.23.2.123.

Pearson, P. N., R. K. Olsson, C. Hemblen, B. T. Huber, and W. A. Berggren (Eds.) (2006), *Atlas of Eocene Planktonic Foraminifera*, *Cushman Special Publication*, vol. 41, pp. 513, Department of Geology East Carolina Univ., Greenville.

Perch-Nielsen, K. (1981), Nouvelles observations sur les nannofossiles calcaires a la limite Cretace-Tertiaire pres de El Kef, Tunisie, *Cahiers de Micropaléontol.*, *3*, 25–36.

Petrizzo, M.-R., G. Leoni, R. P. Speijer, B. De Bernardi, and F. Felletti (2008), Dissolution susceptibility of some Paleogene planktonic foraminifera from ODP Site 1209 (Shatsky Rise, Pacific Ocean), *J. Foraminiferal Res.*, *38*(4), 357–371.

Premoli Silva, I., and A. Boersma (1988), Atlantic Eocene planktonic foraminiferal historical biogeography and paleohydrographic indices, *Palaeogeogr. Palaeoclimatol. Palaeoecol.*, *67*(3-4), 315–356, doi:10.1016/0031-0182(88)90159-9.

Premoli Silva, I., and A. Boersma (1989), Atlantic Paleogene planktonic foraminiferal bioprovincial indices, *Mar. Micropaleontol.*, *14*(4), 357–372, doi:10.1016/0377-8398(89)90019-4.

Quillévéré, F., R. D. Norris, I. Moussa, and W. A. Berggren (2001), Role of photosymbiosis and biogeography in the diversification of early Paleogene acarininids (planktonic foraminifera), *Paleobiology*, *27*(2), 311–326, doi:10.1666/0094-8373(2001)027<0311:ROPABI>2.0.CO;2.

Rio, D., I. Raffi, and G. Villa (1990a), Pliocene-Pleistocene calcareous nannofossili distribution patterns in the western Mediterranean, in *Proceedings of the Ocean Drilling Program, Scientific Results*, edited by K. A. Kasterns et al., 107, 513-533, Ocean Drill. Program, College Station, Tex., doi:10.2973/odp.proc.sr.107.164.1990.

Rio, D., Fornaciari, E. and I. Raffi (1990b), Late Oligocene through early Pleistoene calcareous nannofossils from western equatorial Indian Ocean (Leg 115), in *Proceedings of the Ocean Drilling Program, Scientific Results*, 115, edited by R. A. Duncan et al., 175–235, Ocean Drilling Program, College Station, TX, USA, doi:10.2973/odp.proc.sr.115.152.1990.

Röhl, U., T. Westerhold, S. Monechi, E. Thomas, J. C. Zachos, and B. Donner (2005), The third and final early Eocene Thermal Maximum: Characteristics, timing, and mechanisms of the "X" event, *Geol. Soc. Am. Abstr. Program*, *37*(7), 264.

Röhl, U., T. Westerhold, T. J. Bralower, and J. C. Zachos (2007), On the duration of the Paleocene-Eocene thermal maximum (PETM), *Geochem. Geophys. Geosyst.*, *8*, Q12002, doi:10.1029/2007GC001784.

Roth, P. H. (1983), Jurassic and Lower Cretaceous calcareous nannofossils in the western North Atlantic (Site 534): Biostratigraphy, preservation, and some observations on biogeography and paleoceanography, in *Deep Sea Drilling Project, Initial Reports*., 76, edited by R. E. Sheridan et al., 587-621, U.S. Gov. Print. Off., Washington, D. C., doi:10.2973/dsdp.proc.76.125.1983.

Roth, P. H., and H. Thierstein (1972), Calcareous nannoplankton: Leg 14 of the Deep Sea Drilling Project, in *Deep Sea Drilling Project, Initial Reports*., 14, edited by D. E. Hayes et al., 421-485, U.S. Gov. Print. Off., Washington, D. C., doi:10.2973/dsdp.proc.14.1972.

Schmidt, D. N., S. Renaud, J. Bollmann, R. Schiebel, and H. R. Thierstein (2004), Size distribution of Holocene planktic foraminifer assemblages: Biogeography, ecology and adaptation, *Mar. Micropaleont.*, *50*(3–4), 319–338, doi:10.1016/S0377-8398(03)00098-7.

Schmidt, D. N., D. Lazarus, J. R. Young, and M. Kucera (2006), Biogeography and evolution of body size in marine plankton, *Earth Sci. Rev.*, *78*, 239–266, doi:10.1016/j.earscirev.2006.05.004.

Schoon, P. L., A. Sluijs, J. S. Sinninghe Damsté, and S. Schouten (2011), High productivity and elevated carbon isotope fractionations in the Arctic Ocean during Eocene Thermal Maximum 2, *Paleoceanography*, *26*, PA3215, doi:10.1029/2010PA002028.

Schrag, D. P., D. J. DePaolo, and F. M. Richter (1995), Reconstructing past sea surface temperatures: Correcting for diagenesis of bulk marine carbonate, *Geochim. Cosmochim. Acta*, *59*, 2265–2278.

Sexton, P. F., R. D. Norris, P. A. Wilson, H. Pälike, T. Westerhold, U. Röhl, C. T. Bolton, and S. J. Gibbs (2011), Eocene global warming events driven by ventilation of oceanic dissolved organic carbon, *Nature*, *471*(7338), 349–352, doi:10.1038/nature09826.

Slotnick, B. S., G. R. Dickens, M. J. Nicolo, C. J. Hollis, J. S. Crampton, and J. C. Zachos (2012), Large-amplitude variations in carbon cycling and terrestrial weathering during the latest Paleocene and earliest Eocene: The record at Mead Stream, New Zealand, *J. Geol.*, *120*(5), 487–505, doi:10.1086/666743.

Sluijs, A., S. Schouten, T. H. Donders, P. L. Schoon, U. Röhl, G.-J. Reichart, F. Sangiorgi, J. H. Kim, J. S. Sinninghe Damsté, and H. Brinkhuis (2009), Warm and wet conditions in the Arctic region during Eocene Thermal Maximum 2, *Nat. Geosci.*, *2*(11), 1–4, doi:10.1038/ngeo668.

Speijer, R. P., and B. Schmitz (1998), A benthic foraminiferal record of Paleocene sea level and trophic/redox conditions at Gebel Aweina, Egypt, *Palaeogeogr. Palaeoclimatol. Palaeoecol.*, *137*, 79–101.

Spötl, C., and T. W. Vennemann (2003), Continuous-flow isotope ratio mass spectrometric analysis of carbonate minerals, *Rapid Commun. Mass Spectrom.*, *17*(9), 1004–1006, doi:10.1002/rcm.1010.

Stap, L., A. Sluijs, E. Thomas, and L. J. Lourens (2009), Patterns and magnitude of deep sea carbonate dissolution during Eocene Thermal Maximum 2 and H2, Walvis Ridge, Southeastern Atlantic Ocean, *Paleoceanography*, *24*, PA1211, doi:10.1029/2008PA001655.

Stap, L., L. J. Lourens, E. Thomas, A. Sluijs, S. Bohaty, and J. C. Zachos (2010a), High-resolution deep-sea carbon and oxygen isotope records of Eocene Thermal Maximum 2 and H2, *Geology*, *38*, 607–610, doi:10.1130/G30777.1.

Stap, L., L. J. Lourens, A. van Dijk, S. Schouten, and E. Thomas (2010b), Coherent pattern and timing of the carbon isotope excursion and warming during Eocene Thermal Maximum 2 as recorded in planktic and benthic foraminifera, *Geochem. Geophys. Geosyst.*, *11*, Q11011, doi:10.1029/2010GC003097.

Stassen, P., E. Steurbaut, A.-M. M. Morsi, P. Schulte, and R. P. Speijer (2012), Biotic impact of Eocene Thermal Maximum 2 in a shelf setting (Dababiya, Egypt), *Austrian J. Earth Sci.*, *105*(1), 154–160.

Suganuma, Y., and J. G. Ogg (2006), Campanian through Eocene magnetostratigraphy of sites 1257–1261, ODP leg 207, Demerara rise (Western Equatorial Atlantic), in *Proceedings of the Ocean Drilling Program, Scientific Results*, 207, 1-48, Ocean Drill. Program, College Station, Tex., [Available at http://www-odp.tamu.edu/publications/207_SR/102/102.htm.]

Thierstein, H. R., K. R. Geitzenauer, and B. Molfino (1977), Global synchroneit of late Quaternary coccolith datum levels: Validation by oxigen isotopes, *Geol. Soc. Am.*, *5*, 400–404.

Thomas, E., J. C. Zachos, and T. J. Bralower (2000), Deep-sea environments on a warm earth: latest Paleocene–early Eocene, in *Warm Climates in Earth History*, edited by B. Huber, K. MacLeod, and S. Wing, pp. 132–160, Cambridge Univ. Press, Cambridge, U. K.

Thomas, E., H. Brinkhuis, M. Huber, and U. Röhl (2006), An ocean view of the early Cenozoic greenhouse world, *Oceanography*, *19*, 63–72.

Thunell, R. C., and S. Honjo (1981), Calcite dissolution and the modification of planktonic foraminiferal assemblages, *Mar. Micropaleontol.*, *6*(2), 169–182.

Tjalsma, R. C., and G. P. Lohmann (1983), Paleocene-Eocene bathyal and abyssal benthic foraminifera from the Atlantic Ocean, *Micropaleontol. Spec. Publ.*, *4*, 1–90.

Toffanin, F., C. Agnini, E. Fornaciari, D. Rio, L. Giusberti, V. Luciani, D. J. A. Spofforth, and H. Pälike (2011), Changes in calcareous nannofossil assemblages during the Middle Eocene Climatic Optimum: Clues from the central-western Tethys (Alano section, NE Italy), *Mar. Micropaleontol.*, *81*(1), 22–31, doi:10.1016/j.marmicro.2011.07.002.

Tremolada, F., and T. J. Bralower (2004), Nannofossil assemblage fluctuations during the Paleocene-Eocene thermal maximum at Sites 213 (Indian Ocean) and 401 (North Atlantic Ocean): Palaeoceanographic implications, *Mar. Micropaleontol.*, *52*(1), 107–116, doi:10.1016/j.marmicro.2004.04.002.

Van der Zwaan, G. J., F. J. Jorissen, and H. C. De Stigter (1990), The depth dependency of planktic/benthonic foraminiferal ratios: Constraints and applications, *Mar. Geol.*, *95*, 1–16.

Van Hinsbergen, D. J. J., L. V. de Groot, S. J., van Schaik, W. Spakman, P. K. Bijl, A. Sluijs, C. G. Langereis, and H. Brinkhuis (2015), A Paleolatitude Calculator for Paleoclimate Studies, *PLoS ONE*, *10*, e0126946, doi:10.1371/journal.pone.0126946.

Van Morkhoven, F. P. C. M., W. A. Berggren, and A. S. Edwards (1986), Cenozoic Cosmopolitan deep-sea benthic foraminifera, *Bull. des Centres de Recherches Exploration-Production Elf-Aquitane, Mèmoire*, *11*, 11–421.

Villa, G., C. Fioroni, L. Pea, S. M. Bohaty, and D. Persico (2008), Middle Eocene–late Oligocene climate variability: Calcareous nannofossil response at Kerguelen Plateau, Site 748, *Mar. Micropaleontol.*, *69*, 173–192.

Wade, B. S., and R. K. Olsson (2009), Investigation of pre-extinction dwarfing in Cenozoic planktonic foraminifera, *Palaeogeogr. Palaeoclimatol. Palaeoecol.*, *284*, 39–46.

Wade, B. S., N. Al-Sabouni, C. Hemleben, and D. Kroon (2008), Symbiont bleaching in fossil planktonic foraminifera, *Evol. Ecol.*, *22*(2), 253–265, doi:10.1007/s10682-007-9176-6.

Wade, B. S., P. N. Pearson, W. A. Berggren, and H. Pälike (2011), Review and revision of Cenozoic tropical planktonic foraminiferal biostratigraphy and calibration to the geomagnetic polarity and astronomical time scale, *Earth Sci. Rev.*, *104*(1-3), 111–142, doi:10.1016/j.earscirev.2010.09.003.

Watson, G. (1983), Large sample theory of the Langevin distribution, *J. Stat. Plan. Inference*, *8*, 245–256.

Wei, W., and S. W. Wise Jr. (1990), Biogeographic gradients of middle Eocene–Oligocene calcareous nannoplankton in the South Atlantic Ocean, *Palaeogeogr. Palaeoclimatol. Palaeoecol.*, *79*, 29–61.

Westerhold, T., and U. Röhl (2009), High resolution cyclostratigraphy of the early Eocene—New insights into the origin of the Cenozoic cooling trend, *Clim. Past*, *5*(3), 309–327, doi:10.5194/cp-5-309-2009.

Westerhold, T., U. Röhl, J. Laskar, I. Raffi, J. Bowles, L. J. Lourens, and J. C. Zachos (2007), On the duration of magnetochrons C24r and C25n and the timing of early Eocene global warming events: Implications from the Ocean Drilling Program Leg 208 Walvis Ridge depth transect, *Paleoceanography*, *22*, PA2201, doi:10.1029/2006PA001322.

Westerhold, T., U. Röhl, I. Raffi, E. Fornaciari, S. Monechi, V. Reale, J. Bowles, and H. F. Evans (2008), Astronomical calibration of the Paleocene time, *Palaeogeogr. Palaeoclimatol. Palaeoecol.*, *257*, 377–403, doi:10.1016/j.palaeo.2007.09.016.

Westerhold, T., U. Röhl, and J. Laskar (2012), Time scale controversy: Accurate orbital calibration of the early Paleogene, *Geochem. Geophys. Geosyst.*, *13*, Q06015, doi:10.1029/2012GC004096.

Westerhold, T., U. Röhl, T. Frederichs, S. M. Bohaty, and J. C. Zachos (2015), Astronomical calibration of the geological timescale: Closing the middle Eocene gap, *Clim. Past*, *11*(9), 1181–1195, doi:10.5194/cp-11-1181-2015.

Young, J. R. (1994), Functions of coccoliths, in *Coccolithophores*, edited by A. Winter and W. G. Siesser, pp. 63–82, Cambridge Univ. Press, Cambridge.

Zachos, J. C., et al. (2005), Rapid acidification of the ocean during the Paleocene-Eocene thermal maximum, *Science*, *308*, 1611–1615, doi:10.1126/science.1109004.

Zachos, J. C., G. R. Dickens, and R. E. Zeebe (2008), An early Cenozoic perspective on greenhouse warming and carbon-cycle dynamics, *Nature*, *451*(7176), 279-283, doi:10.1038/nature06588.

Zachos, J. C., H. K. McCarren, B. Murphy, U. Röhl, and T. Westerhold (2010), Tempo and scale of late Paleocene and early Eocene carbon isotope cycles: Implications for the origin of hyperthermals, *Earth Planet. Sci. Lett.*, *299*, 242–249, doi:10.1016/j.epsl.2010.09.004.

Zeebe, R. E., J. C. Zachos, and G. R. Dickens (2009), Carbon dioxide forcing alone insufficient to explain Palaeocene–Eocene Thermal Maximum warming, *Nat. Geosci.*, *2*(8), 576–580, doi:10.1038/ngeo578.

Zijderveld, J. D. A. (1967), A.C. demagnetization of rocks: analysis of results, in *Methods in Paleomagnetism*, vol. 3, edited by D. W. Collinson, K. M. Creer, and S. K. Runcorn, pp. 254–286, Elsevier, Amsterdam.